Nano Research

ISSN 1998-0124 CN 11-5974/O4
https://doi.org/10.26599/NR.2026.94909316

Research Article

Ultra-low-temperature seawater zinc–air batteries enabled by carbon nanochannel-confined high-entropy alloy catalysts

Hucheng Song[1](✉), Yixin Liu[1], Deen Li[1], Xilei Ding[1], Min Wang[2], Yuzi Zhang[1], Changshun Wang[1](✉), Jing Wu[1](✉), Guangbin Zhang[1](✉), Jun Xu[2,3]

[1] School of Physics, Nanjing University of Aeronautics and Astronautics, Nanjing 211106, China

[2] School of Electronics Science and Engineering, National Laboratory of Solid State Microstructures, Nanjing University, Nanjing 210093, China

[3] School of Microelectronics, School of Physics, Nantong University 226019, China

Nano Res., **Just Accepted Manuscript** • https://doi.org/10.26599/NR.2026.94909316

https://www.sciopen.com/journal/1998-0124 on Nov. 9, 2026

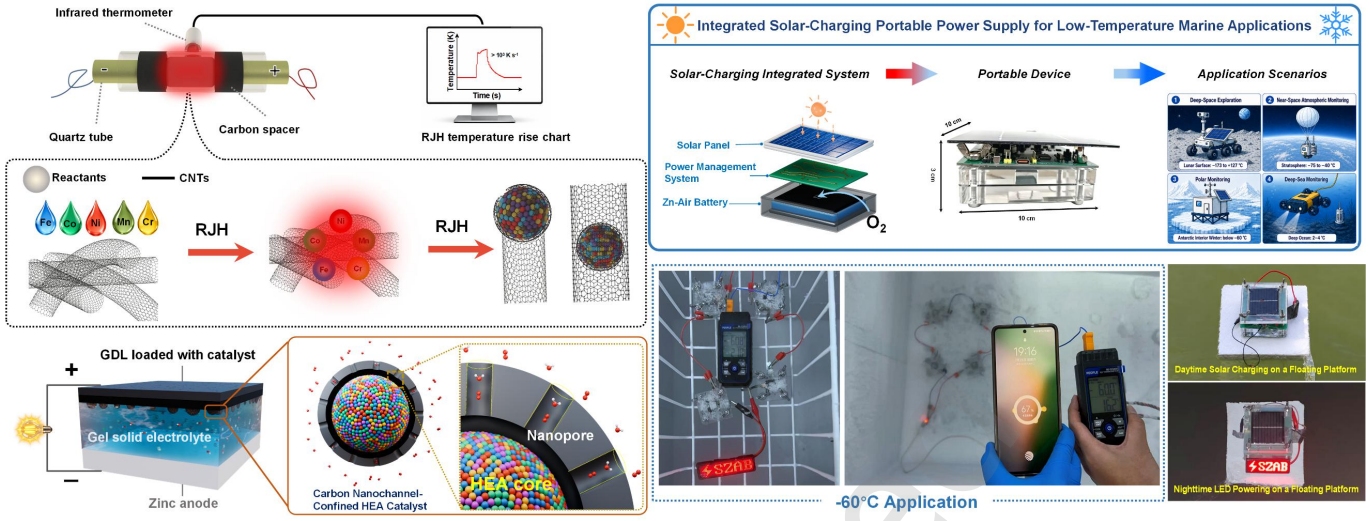
© The Authors(s)

Just Accepted

This is a "Just Accepted" manuscript, which has been examined by the peer-review process and has been accepted for publication. A "Just Accepted" manuscript is published online shortly after its acceptance,which is prior to technical editing and formatting and author proofing. Tsinghua University Press (TUP) provides "Just Accepted" as an optional and free service which allows authors to make their results available to the research community as soon as possible after acceptance. After a manuscript has been technically edited and formatted, and the page proofs have been corrected, it will be removed from the "Just Accepted" web site and published officially with volume and article number (e.g., *Nano Research*, **2025**, *18*, 94906990). Please note that technical editing may introduce minor changes to the manuscript text and/or graphics which may affect the content, and all legal disclaimers that apply to the journal pertain. In no event shall TUP be held responsible for errors or consequences arising from the use of any information contained in these "Just Accepted" manuscripts. To cite this anuscript please use its Digital Object Identifier (DOI®),which is identical for all formats of publication.

Just Accepted

TABLE OF CONTENTS (TOC)



1. A carbon-nanochannel-confined Fe-Co-Ni-Mn-Cr high-entropy alloy catalyst enables a seawater-mimetic hydrogel zinc–air battery that delivers a peak power density of 407.82 mW cm^{-2} and a specific capacity of 664.2 mAh gZn^{-1} at 25 °C, and cycles stably for more than 800 cycles at −60 °C.
2. An integrated solar-rechargeable pack powers LEDs and a smartphone at −60 °C, demonstrating practical cryogenic energy storage for marine and polar environments.

Just Accepted

Research Article

Ultra-low-temperature seawater zinc–air batteries enabled by carbon nanochannel-confined high-entropy alloy catalysts

Hucheng Song [1], Yixin Liu [1], Deen Li [1], Xilei Ding [1], Min Wang [2], Yuzi Zhang [1], Changshun Wang [1], Jing Wu [1], Guangbin Zhang [1], Jun Xu [2,3]

[1] School of Physics, Nanjing University of Aeronautics and Astronautics, Nanjing 211106, China
[2] School of Electronics Science and Engineering, National Laboratory of Solid State Microstructures, Nanjing University, Nanjing 210093, China
[3] School of Microelectronics, School of Physics, Nantong University 226019, China

Received: 19 September 2026; **Revised: 19 October 2026**; **Accepted: 9 November 2026**

Address correspondence to Hucheng Song, hcsong@nuaa.edu.cn; Changshun Wang, changshun@nuaa.edu.cn; Jing Wu, jingwu22@nuaa.edu.cn; Guangbin Zhang, zhgb2007@nuaa.edu.cn

Cite this article: *Nano Research*, 2027, 20, 94909316 https://doi.org/10.26599/NR.2026.94909316

ABSTRACT: Seawater-based solid-state zinc–air batteries are attractive for extreme-environment applications because of their high energy density, intrinsic safety, low-temperature operability, and in situ resource utilization. However, sluggish cathodic oxygen redox kinetics at low temperatures and catalyst degradation in strongly alkaline seawater severely compromise their energy efficiency and cycling stability. We synthesized a noble-metal-free high-entropy alloy (HEA) nanoparticle catalyst with carbon nanochannel confinement by rapid Joule heating. The resulting catalyst couples this physical confinement with the distinctive electronic structure of the HEA. Molecular dynamics simulations show that this confinement increases the local probability of finding O_2 and OH^- near the catalyst surface, creating a favorable interfacial environment for oxygen redox reactions at low temperatures. Structural characterizations reveal that the confined carbon architecture limits direct exposure of the HEA to the alkaline chloride-containing electrolyte. The resulting seawater-mimetic hydrogel solid-state zinc–air battery, prepared with 8 M KOH containing 3.1 wt% NaCl, delivers a peak power density of 407.82 mW cm^{-2} and a specific capacity of 664.2 mAh g_{Zn}^{-1} at room temperature. It operates stably for over 800 cycles at −60 °C and 8 mA cm^{-2} while 1.4–3.1 wt% NaCl cells remain reversible at −60 °C; 7.0 wt% NaCl is a high-salinity stress condition that fails after 68 cycles. A solar-rechargeable battery powers a smartphone and an LED array at −60 °C, demonstrating reliable cryogenic operation and offering a practical route to salinity-tolerant low-temperature solid-state batteries.

KEYWORDS: solid-state battery, zinc–air battery, high-entropy alloy, nano confinement, seawater-based battery, low-temperature battery

Just Accepted

1 Instruction

As conventional resources become increasingly scarce, the abundant resources available in extreme environments, including the deep sea, deep space, deep earth, and polar regions, have attracted growing research interest [1, 2]. Exploiting these environments requires energy storage devices that operate reliably under harsh conditions [1, 3]. Such applications demand electrochemical energy storage systems that provide not only high energy density and intrinsic safety but also dependable performance over a wide temperature window, particularly at ultra-low temperatures from room temperature down to −60 °C and below, as needed for deep-sea exploration, deep-earth probing, polar missions, and deep-space exploration [1, 4-6]. Moreover, the ability to harness in situ resources, such as atmospheric O_2 in near space or at high altitude and seawater containing dissolved O_2 in deep-sea settings, has become a decisive advantage for sustainable energy supply in remote and isolated missions [7-9]. Among the diverse electrochemical energy storage technologies, aqueous zinc–air batteries (ZABs) stand out owing to their high theoretical energy density (1086 Wh kg^{-1}), intrinsic safety, environmental benignity, and remarkable in situ resource utilization capability [10-12]. This capability stems from their ability to directly consume O_2 as the cathodic reactant while employing seawater-derived electrolytes for ionic transport.

In particular, solid-state ZABs based on hydrogel electrolytes have emerged as an attractive configuration because they minimize leakage risk, suppress zinc dendrite growth, and offer superior mechanical flexibility [13, 14]. Incorporating highly concentrated alkaline salts (e.g., 6–12 M KOH or KAc) into polymer matrices such as poly(acrylamide-co-acrylic acid) (P(AM-co-AA)) or poly(vinyl alcohol) (PVA) disrupts the hydrogen-bonding network of water, which imparts exceptional anti-freezing capability and enables battery operation at subzero temperatures [4, 6, 15-19]. For instance, Pei et al. developed an alkalified poly(acrylic acid) (A-PAA) hydrogel electrolyte containing 30 wt% KOH that enabled rechargeable flexible ZABs to maintain stable charge–discharge behavior at −20 °C [20]. Zhang et al. subsequently developed a PAM-CNF/KOH/KI

double-network hydrogel electrolyte that enabled flexible ZABs to operate reliably at −40 °C while retaining a specific capacity of approximately 743 mAh g^{-1} and a maximum power density of 10 mW cm^{-2} [21]. Zhong et al. introduced the hygroscopic ionic liquid 1-ethyl-3-methylimidazolium chloride (EMImCl) into a poly(sodium acrylate)–poly(vinyl alcohol) (PANa–PVA) hydrogel containing 6 M KOH and 0.2 M $Zn(Ac)_2$, enabling flexible ZAB operation across a wide temperature range from −40 to 60 °C with a charge–discharge voltage gap of approximately 1.1 V at −40 °C [22]. Despite these advances, sluggish oxygen reduction/oxygen evolution reaction (ORR/OER) kinetics at low temperatures and progressive degradation of the air cathode under strongly alkaline and oxidative charging conditions remain critical limitations for the energy efficiency and cycling stability of solid-state ZABs [5, 23-25].

To accelerate the cathodic oxygen reduction and evolution kinetics, noble-metal-based catalysts such as Pt/C and IrO_2 /RuO_2 have long been established as benchmark bifunctional oxygen electrocatalysts owing to their superior ORR/OER activity [26, 27]. However, their prohibitive cost, elemental scarcity, and insufficient durability in strongly alkaline and low-temperature environments severely hinder their scalable deployment in solid-state ZABs [24, 27, 28]. In response, non-noble-metal catalysts have attracted intensive research interest because of their elemental abundance and economic viability [27, 29]. Among them, high-entropy alloy (HEA) catalysts composed of five or more metallic elements in near-equimolar ratios have emerged as a particularly prominent class: their multicomponent synergistic effects, diverse local coordination environments, and continuously tunable electronic structures optimize the adsorption energetics of oxygen-containing intermediates and thereby enhance bifunctional ORR/OER activity [30-32]. For instance, Yen et al. developed a CrMnFeCoNi–CrO_x heterostructured catalyst that enabled rechargeable ZABs to operate stably for 765 h at 10 mA cm^{-2}, while maintaining an initial charge–discharge voltage gap of approximately 0.78 V at room temperature [33]. Similarly, Xia et al. confined FeCoNiCrMn HEA nanoparticles within electrospun carbon nanofibers, enabling flexible ZABs to achieve a specific capacity of 826 mAh g_{Zn}^{-1} and stable cycling for over 88 h at 5 mA cm^{-2} [34]. Qiu et al. developed a dealloyed nanoporous AlNiCoFeMo HEA covered with high-entropy (oxy)hydroxides that required an OER overpotential of only 240 mV to reach 10 mA cm^{-2} in 1 M KOH, demonstrating the effectiveness of multicomponent and nanoporous engineering in reducing OER polarization [35]. Despite these advances, HEA catalysts still suffer from sluggish reaction kinetics at low temperatures and remain susceptible to corrosion and surface reconstruction in strongly alkaline environments [36-38]. Maintaining high activity while preserving structural stability therefore remains a critical challenge.

To mitigate catalyst degradation, carbon-shell encapsulation has proven to be an effective strategy. Ultrathin graphene or N-doped carbon shells physically isolate the metallic core from the corrosive electrolyte while allowing the electronic influence of the encapsulated metal to penetrate the carbon layer and modulate the surface-active sites, thereby enhancing both catalytic activity and structural durability [39-41]. Similarly, Miao et al. encapsulated FeNi alloy nanoparticles within N-doped carbon shells, which physically protected the metallic core from corrosion while maintaining efficient ORR/OER activity, enabling an all-solid-state ZAB with an open-circuit voltage of 1.394 V and a peak power density of 59.7 mW cm^{-2} [42]. Wang et al. encapsulated Co_9Se_8 nanoparticles within ultrathin carbon-chainmail shells on N-doped mesoporous carbon. The carbon shell acted as a protective barrier that suppressed Cl^- adsorption while maintaining efficient electron transport, enabling seawater-based ZABs to sustain stable charge–discharge cycling for over 200 h [43]. In addition, alloying with corrosion-resistant elements such as Cr promotes the formation of protective oxide/oxyhydroxide layers. Constructing strong metal–support interactions can also anchor active species, suppress their dissolution and agglomeration, and thereby enhance structural stability during prolonged cycling [44, 45]. Collectively, developing non-noble-metal catalysts that combine high intrinsic activity with robust tolerance to strong alkali and low temperatures is essential for energy-efficient, long-life, low-temperature solid-state ZABs.

Beyond low-temperature operability, the use of seawater-mimetic saline electrolytes offers another compelling route to in situ resource utilization, reducing freshwater dependence and enhancing energy self-sufficiency in marine environments [11, 12]. Seawater-based ZABs, however, are constrained by high Cl^- concentrations (~0.5 M) and other impurity ions that accelerate catalyst corrosion [9, 43, 46, 47]. Although protective carbon shells or nitrogen-doped coatings have been employed to suppress Cl^- attack, cathodic kinetics remain sluggish, and the low dissolved oxygen concentration further exacerbates mass-transport limitations, severely restricting their development [48-50]. In this work, "seawater-mimetic" refers to an 8 M KOH hydrogel containing 1.4–7.0 wt% NaCl; natural seawater was not used.

Here, we report a salinity-tolerant, seawater-mimetic hydrogel zinc–air battery capable of operating down to −60 °C. A noble-metal-free Fe-Co-Ni-Mn-Cr HEA oxygen electrocatalyst was synthesized by rapid Joule heating (RJH), producing HEA nanoparticles (predominantly 30–60 nm) that are either partially encapsulated by few-layer porous graphene shells at the open ends of the carbon nanotubes or confined within the interiors of the nanotube channels. This hierarchical carbon nanoconfinement combines a permeable protective interface with continuous pathways for electron transport and O_2 /OH^- diffusion, thereby stabilizing the alloy nanoparticles in alkaline chloride-containing media. Molecular dynamics simulations further reveal a higher local probability of finding O_2 and OH^- near the catalyst surface under confinement, suggesting enhanced interfacial availability of oxygen-redox species at low temperature. In an 8 M KOH hydrogel containing 3.1 wt% NaCl, the battery delivers a peak power density of 407.82 mW cm^{-2} and a specific capacity of 664.2 mAh g_{Zn}^{-1} at 25 °C, while retaining 62.67 mW cm^{-2} and 371.0 mAh g_{Zn}^{-1}, respectively, at −40 °C. It maintains stable cycling for 400 cycles at 25 °C and more than 800 cycles at −60 °C under 8 mA cm^{-2}. Batteries assembled with fixed NaCl concentrations of 1.4, 2.0 and 3.1 wt% sustain reversible operation with voltage gaps remaining below 1.0 V at 25 °C and below 2.0 V at −60 °C, whereas the cell containing 7.0 wt% NaCl fails after 301 cycles at 25 °C and after only 68 cycles at −60 °C. Finally, an integrated solar-rechargeable battery pack powers an LED array and charges a commercial smartphone at −60 °C, demonstrating

Just Accepted

a viable device-level strategy for salinity-tolerant energy storage in cold marine and polar environments.

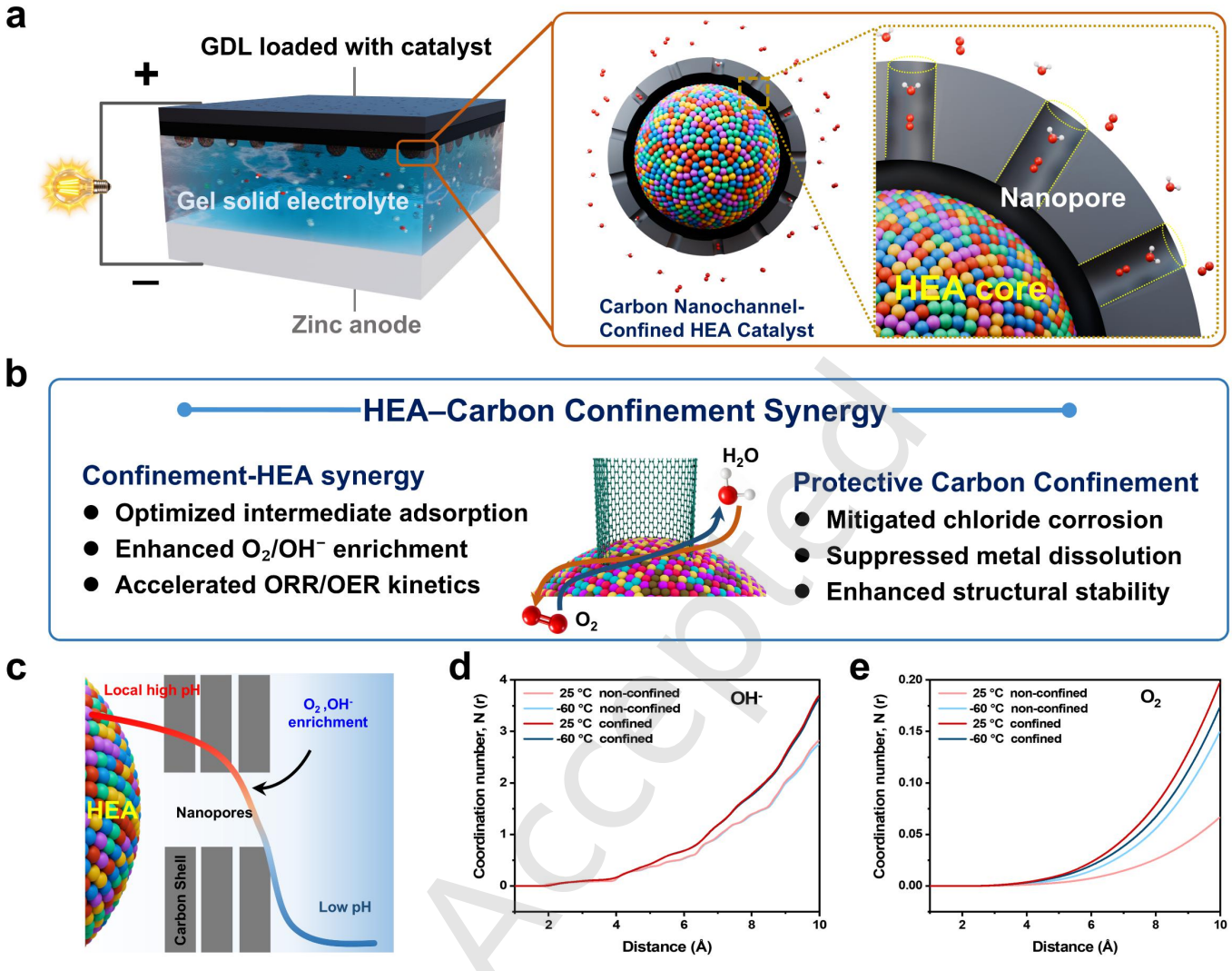


Figure 1. Design and interfacial characteristics of the carbon nanochannel-confined HEA catalyst. (a) Schematic of the seawater-mimetic hydrogel Zn–air battery (left) and enlarged structure of the carbon nanochannel-confined HEA catalyst loaded on the gas-diffusion layer (right). (b) Synergy between the HEA catalyst and protective carbon confinement. (c) Local interfacial environment and transport of O_2 and OH^- through the carbon-shell nanopores. (d, e) Coordination-number profiles of OH^- (d) and O_2 (e) around the HEA under confined and non-confined conditions at both 25 and −60 °C.

2 Result and Discussion

2.1 *Design and Interfacial Regulation of the Carbon Nanochannel-Confined HEA Catalyst*

Figure 1 illustrates the design rationale of the carbon nanochannel-confined high-entropy alloy (HEA) catalyst for gel-electrolyte zinc–air batteries. Integrated into the gas-diffusion layer (GDL), the catalyst consists of a multimetallic HEA core surrounded by a nanoporous carbon shell (Figure 1a). Rather than completely isolating the HEA, the shell creates an interconnected confined space that communicates with the bulk electrolyte through carbon nanochannels, thereby permitting the transport of O_2 , H_2 O and OH^- to and from the catalytic interface. This architecture couples the compositionally diverse HEA surface with a spatially regulated reaction microenvironment. The multimetallic surface provides heterogeneous coordination sites that may modulate the adsorption energetics of oxygenated intermediates, while the accessible confined space promotes retention of reactive species and mitigates their depletion from the catalyst surface. Their cooperative action is therefore expected to facilitate the oxygen reduction and oxygen evolution reactions (ORR/OER; Figure 1b).

In addition to regulating the reaction microenvironment, the carbon shell limits direct exposure of the HEA to the electrolyte and reduces the probability and flux of Cl^- reaching the metal surface (Figure 1c). This semi-permeable interface reduces the probability and flux of Cl^- reaching the metal surface, rather than completely excluding Cl^- , thereby improving the structural stability of the multicomponent alloy during repeated operation. Meanwhile, restricted molecular diffusion within the inner space favors retention of OH^- near the HEA surface, producing a locally OH^- -enriched alkaline environment distinct from the bulk electrolyte. Such interfacial enrichment may become particularly important at low temperatures, where sluggish molecular transport can intensify reactant depletion and kinetic polarization.

To examine the interfacial consequences of this architecture, we performed molecular dynamics (MD) simulations using two structural models: an HEA enclosed within an accessible carbon nanochannel (confined model) and a fully carbon-covered HEA without an accessible confined channel (non-confined model).

Just Accepted

The spatial distributions of O_2 and OH^- around the HEA were evaluated using radial distribution functions, from which cumulative coordination-number profiles were derived (Figure 1d, e). Details of the simulation protocols are provided in the Supplementary Information. At a cutoff radius of 10 Å, the OH^- coordination number at 25 °C increases from approximately 2.90 in the non-confined model to 3.6 under confinement. This difference corresponds to an absolute increase of 0.7 and a relative enhancement of approximately 24%. The enrichment persists at −60 °C, where confinement increases the OH^- coordination number from approximately 2.8 to 3.5—an increase of approximately 25%. The comparable enhancements at the two temperatures demonstrate that the accessible carbon nanochannel consistently increases the average local population of OH^- around the HEA, supporting the formation of an OH^- -enriched interfacial environment even under cryogenic conditions. O_2 shows a species-dependent temperature response (Figure 1e). At 25 °C, the O_2 coordination number within 10 Å of the HEA reaches approximately 0.19 in the confined model, compared with only 0.080 in the non-confined model. Confinement thus increases the local O_2 population by approximately 0.11, equivalent to a 2.4-fold higher local O_2 population (a relative increase of approximately 137%). At −60 °C, the corresponding values are approximately 0.17 and 0.15, respectively, representing a smaller absolute increase of 0.02 and a relative enhancement of approximately 13%. The greater contrast at 25 °C indicates that the accessible nanochannel exerts a particularly pronounced effect on O_2 accumulation under ambient conditions, whereas the difference between the two interfacial configurations becomes less marked at −60 °C. To examine whether the same interfacial confinement also affects Cl^-, we calculated the Cl^- RDF around the HEA using the same reference group and cutoff. The Cl^- RDF at 10 Å decreases by approximately 48% at 25 °C and 76% at −60 °C upon confinement, while the OH^- coordination number increases from 2.9 to 3.6 and from 2.8 to 3.5, respectively (Figure S1). The confined interface is therefore simultaneously enriched in OH^- and depleted in Cl^-. Nevertheless, the higher OH^- coordination number and lower Cl^- RDF in the confined model demonstrate that the carbon shell is not merely a passive coating. Instead, its accessible inner space actively regulates the local availability of reaction species while providing a structural basis for suppressing corrosion and metal dissolution. This dual function establishes the mechanistic foundation for combining efficient oxygen electrocatalysis with enhanced catalyst durability.

2.2 ***Synthesis and Structural Characterization***

Guided by the confinement concept established above, we synthesized the carbon nanochannel-confined Fe-Co-Ni-Mn-Cr HEA catalyst by rapid Joule heating (**Figure 2**a). The Fe, Co, Ni, Mn and Cr precursors were first deposited onto the carbon nanotube (CNT) framework, loaded into a graphite mold, and then subjected to rapid thermal pulses inside a quartz tube, with the transient temperature monitored by an infrared thermometer. The ultrafast heating promotes simultaneous nucleation and interdiffusion of the constituent metals, while the local restructuring of the carbon support produces a graphene shell around the resulting HEA nanoparticles. This process therefore integrates multielement alloying and carbon confinement within a short thermal-treatment period, limiting prolonged particle growth and elemental segregation.

Transmission electron microscopy (TEM) reveals discrete HEA nanoparticles distributed throughout the interconnected CNT network (Figure 2b). Two characteristic configurations are identified: one population nucleates at the open ends of the CNTs, while the other grows within their internal channels. Both populations are associated with a nanoporous few-layer graphene shell, but the tip-anchored particles are only partially covered and are not fully confined by the CNT lumen, whereas the endohedral particles experience additional one-dimensional channel confinement. These observations demonstrate that the catalyst integrates interfacial graphene shell confinement at the CNT openings with one-dimensional confinement inside the CNT channels. The X-ray diffraction (XRD) pattern displays the characteristic (111), (200) and (220) reflections of the Fe-Co-Ni-Mn-Cr alloy, together with the broad (002) reflection of the CNT support (Figure 2c) [32]. The absence of distinguishable diffraction peaks from individual metals or crystalline oxide phases is consistent with the formation of a dominant face-centered-cubic solid-solution phase. Elemental mapping further shows that Cr, Mn, Fe, Co and Ni are spatially co-distributed throughout an individual nanoparticle, without evident element-rich domains (Figure 2d, Figure S2). A carbon signal is also detected over a slightly larger area than that occupied by the metallic elements, forming an envelope around the HEA nanoparticle. The overlapping distributions of the five metallic elements support the formation of a compositionally homogeneous Fe-Co-Ni-Mn-Cr HEA, whereas the extended carbon distribution and the high-resolution TEM (HRTEM) observations confirm that the representative particle is surrounded by a discontinuous few-layer carbon shell; this does not imply that every particle is fully encapsulated.

Under Review

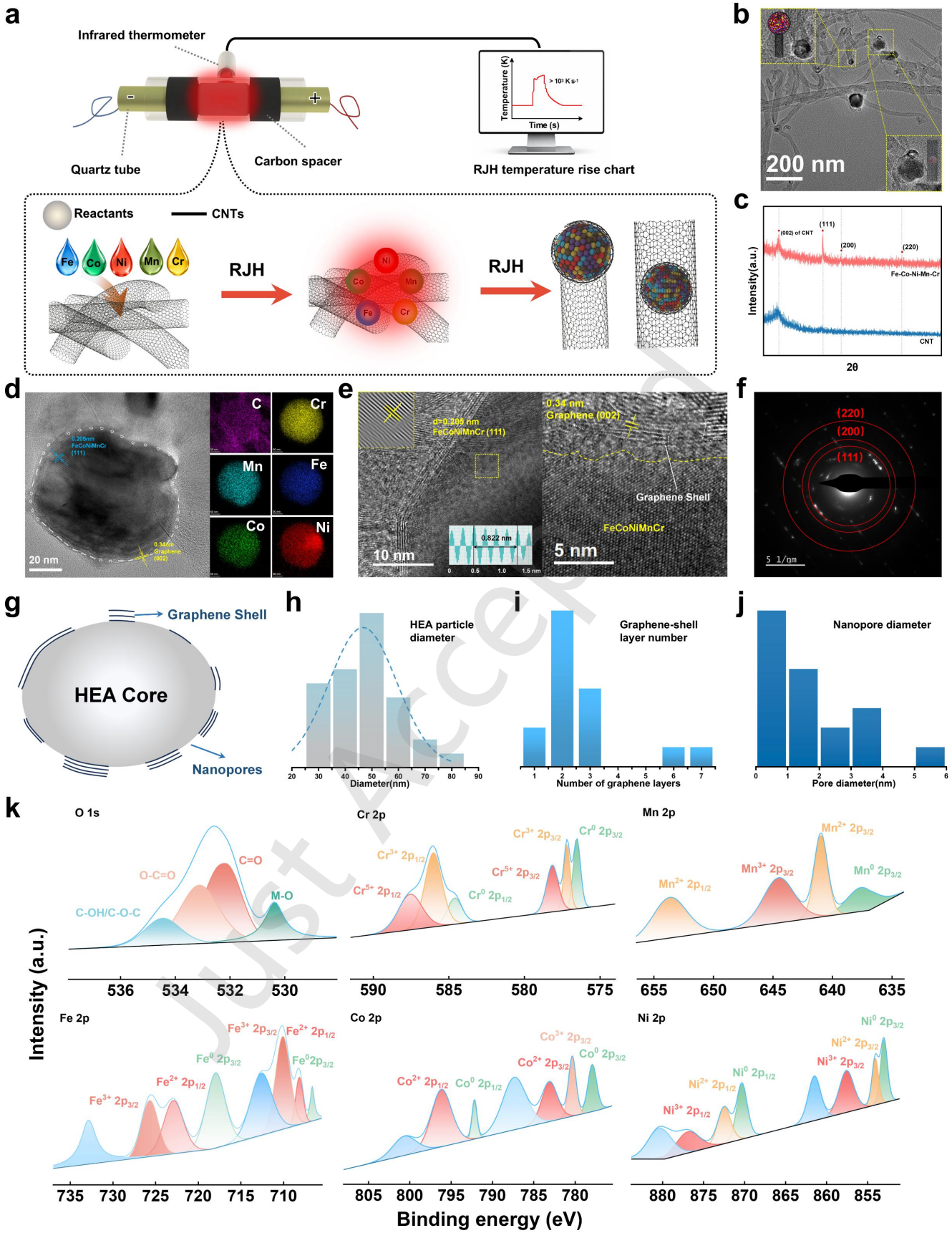


Figure 2. Synthesis and structural characterization of the carbon-confined Fe-Co-Ni-Mn-Cr HEA catalyst. (a) Schematic illustration of the rapid Joule-heating setup and synthesis process. (b) TEM image of both endohedral and tip-anchored HEA particles. (c) XRD patterns of the Fe-Co-Ni-Mn-Cr catalyst and pristine CNTs. (d) TEM image and corresponding elemental mappings of carbon-confined Fe-Co-Ni-Mn-Cr HEA catalyst. (e) HRTEM images of the HEA core and surrounding graphene shell. (f) SAED pattern of the Fe-Co-Ni-Mn-Cr HEA. (g) Schematic illustration of the porous graphene-shell-confined HEA structure. (h), (i), (j) Statistical distributions of HEA particle diameter (h), graphene-shell layer number (i) and nanopore diameter (j). (k) High-resolution O 1s, Cr 2p, Mn 2p, Fe 2p, Co 2p and Ni 2p XPS spectra.

HRTEM provides direct evidence of the alloy–carbon heterointerface (Figure 2e, Figure S3). Within the interior of the

Just Accepted

nanoparticle, lattice fringes with an interplanar spacing of approximately 0.205 nm can be assigned to the (111) plane of Fe-Co-Ni-Mn-Cr HEA (Figure 2e, Figure S4) [51]. By contrast, fringes with a spacing of approximately 0.34 nm are observed at the particle edge and correspond to the graphene (002) plane (Figure 2e, Figure S5) [42]. This spatially resolved lattice assignment provides direct evidence of an Fe-Co-Ni-Mn-Cr HEA core surrounded by a graphitic carbon shell. For the representative particle shown, the close contact between these lattice domains indicates that the HEA core is enclosed by graphitic carbon rather than simply deposited on the external CNT surface; tip-anchored particles may be only partially covered. Consistently, the selected-area electron diffraction (SAED) pattern contains rings indexed to the (111), (200) and (220) planes (Figure 2f), corroborating the crystalline face-centered-cubic structure identified by XRD. The graphene shell is thin and discontinuous, leaving nanoscale openings that connect the HEA surface with the external environment (Figure 2g). Statistical analysis shows that the HEA particles are predominantly 30–60 nm in diameter, with the highest population at approximately 40–50 nm (Figure 2h). Most particles are surrounded by one to three graphene layers, and two-layer shells are the most frequent configuration (Figure 2i). The openings in these shells are primarily 0–2 nm in diameter, although a smaller population of larger pores extending to approximately 6 nm is also present (Figure 2j). This hierarchical opening distribution balances interfacial confinement with molecular accessibility. The sub-2 nm pores may increase the residence time of interfacial species, while the larger openings provide pathways for electrolyte penetration. The shell therefore regulates access rather than acting as a molecular sieve, consistent with the MD results in Figure 1d, e. At the same time, the larger openings provide less restricted pathways for electrolyte penetration, oxygen transport and product removal. The graphene layer therefore functions as a semi-open confinement interface rather than an impermeable encapsulation shell, allowing catalytic accessibility to be maintained while reducing the direct exposure of the HEA core to the corrosive alkaline electrolyte [43].

We subsequently used X-ray photoelectron spectroscopy (XPS) to determine the surface chemical states of the confined catalyst (Figure 2k, Figure S6). The O 1s spectrum can be deconvoluted into components assigned to C–OH/C–O–C, O–C=O, C=O and M–O species at approximately 533.3, 532.4, 531.2 and 529.6 eV, respectively. These signals reveal the coexistence of oxygen-containing carbon functionalities and metal–oxygen interactions at the HEA–carbon interface [51]. The Cr 2p, Mn 2p, Fe 2p, Co 2p and Ni 2p spectra contain both metallic and oxidized components. In particular, the metallic $2p_{3/2}$ signals are located near 574.1 eV for Cr^0, 638.8 eV for Mn^0, 706.8 eV for Fe^0, 778.2 eV for Co^0 and 852.6 eV for Ni^0. The corresponding oxidized components appear at higher binding energies, indicating slight surface oxidation while confirming that the metallic alloy framework is retained [32]. Because XPS primarily probes the upper few nanometres of the material, the oxidized signals should be attributed to surface species rather than complete oxidation of the HEA particles.

Collectively, the structural and spectroscopic results establish a hierarchical catalyst architecture comprising a compositionally homogeneous face-centered-cubic HEA core, a nanoporous few-layer graphene confinement shell and an interconnected CNT conductive framework. The HEA core provides chemically diverse coordination environments, the semi-open graphene shell regulates molecular access while protecting the alloy, and the CNT network supplies continuous electron- and mass-transport pathways. This architecture provides the structural basis for enhancing O_2 /OH^- retention, bifunctional oxygen electrocatalysis and resistance to alkaline corrosion.

Just Accepted

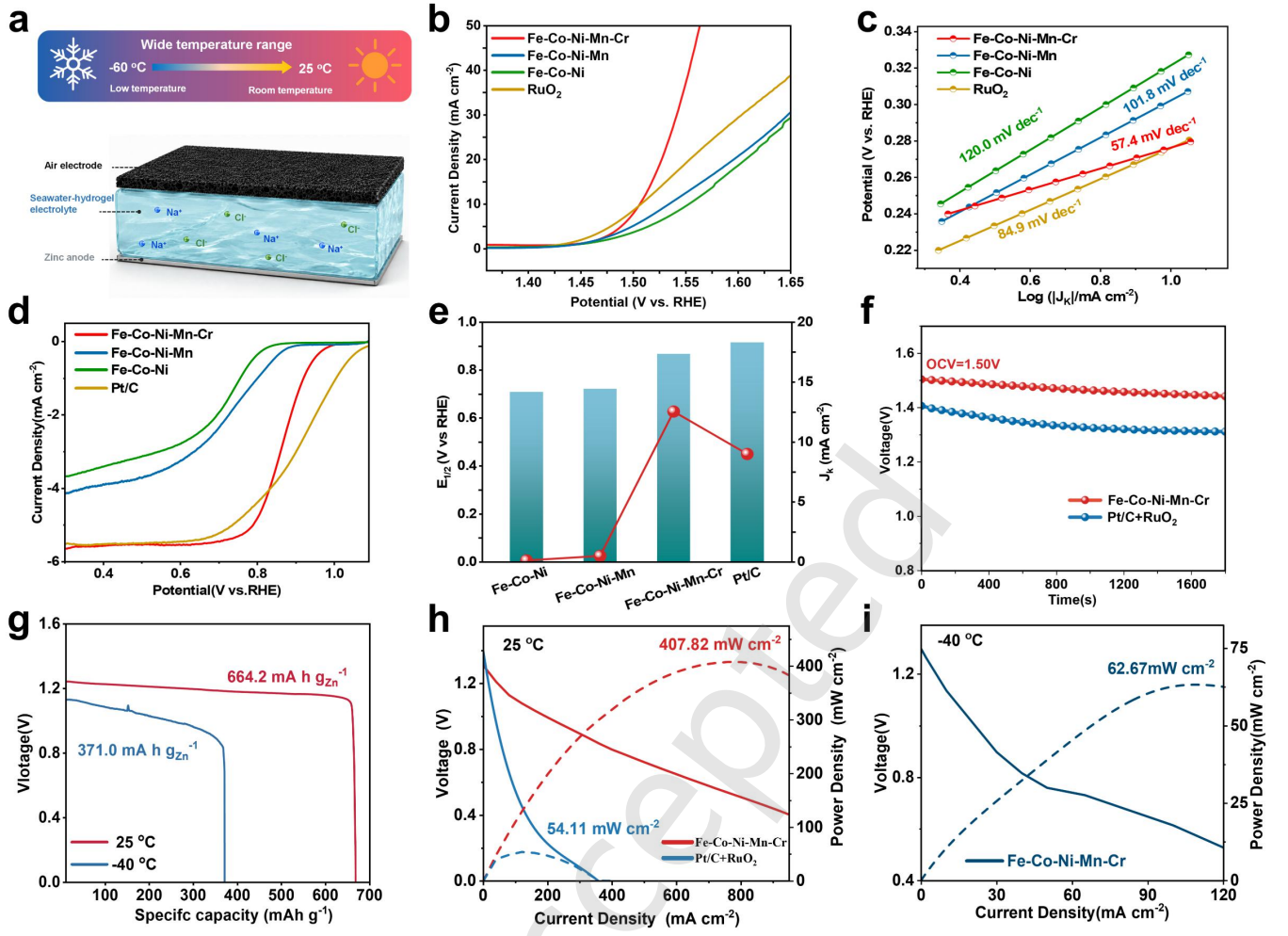


Figure 3. Bifunctional electrocatalytic activity of the Fe-Co-Ni-Mn-Cr HEA catalyst and performance of the corresponding Zn–air battery. (a) Schematic of the seawater-mimetic hydrogel Zn–air battery operating from −60 to 25 °C. (b, c) OER polarization curves and corresponding Tafel plots of Fe-Co-Ni-Mn-Cr, Fe-Co-Ni-Mn, Fe-Co-Ni and RuO_2 . (d, e) ORR polarization curves and comparison of the half-wave potentials and kinetic current densities of the HEA catalysts and Pt/C. (f) Open-circuit voltage profiles of Fe-Co-Ni-Mn-Cr- and Pt/C+RuO_2 -based batteries. (g) Galvanostatic discharge curves of the Fe-Co-Ni-Mn-Cr-based battery at 25 and −40 °C. (h, i) Discharge polarization and power-density curves at 25 and −40 °C, respectively.

2.3 *Bifunctional Oxygen Electrocatalysis and Full-Cell Performance*

We first evaluated the bifunctional oxygen electrocatalytic activity of Fe-Co-Ni-Mn-Cr HEA in a conventional three-electrode system (**Figure 3**). ORR measurements were conducted in O_2 -saturated 0.1 M KOH, whereas OER measurements were performed in 1.0 M KOH. Commercial Pt/C and RuO_2 served as benchmark catalysts for the ORR and OER, respectively. Fe-Co-Ni and Fe-Co-Ni-Mn were examined under identical conditions as compositional controls, allowing the influence of increasing alloy complexity on oxygen electrocatalysis to be assessed. Fe-Co-Ni-Mn-Cr exhibits favourable OER activity, requiring a potential of only 1.506 V to deliver a current density of 10 mA cm^{-2}, which is comparable to and slightly lower than the 1.509 V required by RuO_2 (Figure 3b). More notably, Fe-Co-Ni-Mn-Cr displays a Tafel slope of 57.4 mV dec^{-1}, substantially lower than those of RuO_2 (84.9 mV dec^{-1}), Fe-Co-Ni-Mn (101.8 mV dec^{-1}) and Fe-Co-Ni (120.0 mV dec^{-1}; Figure 3c). The progressive decrease in the Tafel slope from Fe-Co-Ni to Fe-Co-Ni-Mn and Fe-Co-Ni-Mn-Cr indicates that increasing compositional complexity facilitates OER kinetics. The multicomponent HEA surface provides diverse local coordination and electronic environments that may regulate the adsorption and conversion of oxygenated intermediates, while the graphene shells and interconnected CNT framework facilitate electron transport and preserve catalyst–electrolyte accessibility.

The ORR measurements further confirm the compositional advantage of Fe-Co-Ni-Mn-Cr (Figure 3d, e). The half-wave potentials ($E_{1/2}$) of Fe-Co-Ni, Fe-Co-Ni-Mn and Fe-Co-Ni-Mn-Cr are 0.709, 0.721 and 0.867 V versus the reversible hydrogen electrode (RHE), respectively. The $E_{1/2}$ of Fe-Co-Ni-Mn-Cr is therefore markedly more positive than those of its ternary and quaternary counterparts and approaches that of commercial Pt/C (0.915 V versus RHE). An even greater distinction is observed in the kinetic current density. At 0.80 V versus RHE, Fe-Co-Ni-Mn-Cr delivers a kinetic current density of 12.53 mA cm^{-2}, compared with only 0.09 and 0.47 mA cm^{-2} for Fe-Co-Ni and Fe-Co-Ni-Mn, respectively. This value also exceeds that of Pt/C (8.98 mA cm^{-2}) by approximately 40%. Thus, although its half-wave potential remains lower than that of Pt/C, Fe-Co-Ni-Mn-Cr exhibits substantially enhanced reaction kinetics at 0.80 V. Together with its low OER potential and Tafel slope, these results establish Fe-Co-Ni-Mn-Cr as an efficient bifunctional oxygen electrocatalyst. Its performance can be associated with the cooperative effects of the multicomponent alloy surface and hierarchical carbon confinement architecture, which provide diverse catalytic environments, efficient electron transport and accessible reactant pathways.

Just Accepted

We subsequently evaluated the practical functionality of the catalyst by using Fe-Co-Ni-Mn-Cr as the air cathode in a seawater-hydrogel zinc–air battery (Figure 3a). The customized mold used for battery assembly is shown in Figure S7. The assembled battery comprises a Fe-Co-Ni-Mn-Cr air cathode, a hydrogel electrolyte containing KOH and NaCl, and a Zn anode. The Fe-Co-Ni-Mn-Cr-based battery exhibits an initial open-circuit voltage of approximately 1.50 V and retains a voltage of approximately 1.44 V after 1,800 s (Figure 3f). Its open-circuit voltage (OCV) remains consistently higher than that of the Pt/C+RuO_2 -based benchmark battery throughout the measurement, demonstrating effective operation of the confined HEA cathode in the alkaline chloride-containing hydrogel electrolyte. At a discharge current density of 8 mA cm^{-2}, the Fe-Co-Ni-Mn-Cr-based battery delivers a Zn-normalized specific capacity of 664.2 mAh g_{Zn}^{-1} at 25 °C (Figure 3g). When the temperature is lowered to −40 °C, the battery retains a capacity of 371.0 mAh g_{Zn}^{-1}, corresponding to 55.9% of its room-temperature value. The capacity loss at −40 °C can be attributed to the combined effects of reduced ionic conductivity, restricted O_2 transport and increased interfacial reaction resistance. Nevertheless, the substantial retained capacity confirms that reversible electrochemical conversion remains operative under subzero conditions. The power-density measurements further demonstrate the full-cell advantage of the Fe-Co-Ni-Mn-Cr air cathode (Figure 3h, i). At 25 °C, the Fe-Co-Ni-Mn-Cr-based battery reaches a peak power density of 407.82 mW cm^{-2}, approximately 7.5 times the 54.11 mW cm^{-2} obtained with the Pt/C+RuO_2 -based benchmark battery (Figure 3h). Even at −40 °C, it maintains a peak power density of 62.67 mW cm^{-2}, corresponding to 15.4% of its room-temperature value (Figure 3i). Although cooling inevitably decreases the power output because of slower ion transport, O_2 diffusion and interfacial reaction kinetics, the battery retains appreciable capacity and power density at −40 °C. These results demonstrate that the Fe-Co-Ni-Mn-Cr air cathode combines high bifunctional oxygen electrocatalytic activity with effective full-cell operation over a broad temperature range.

Just Accepted

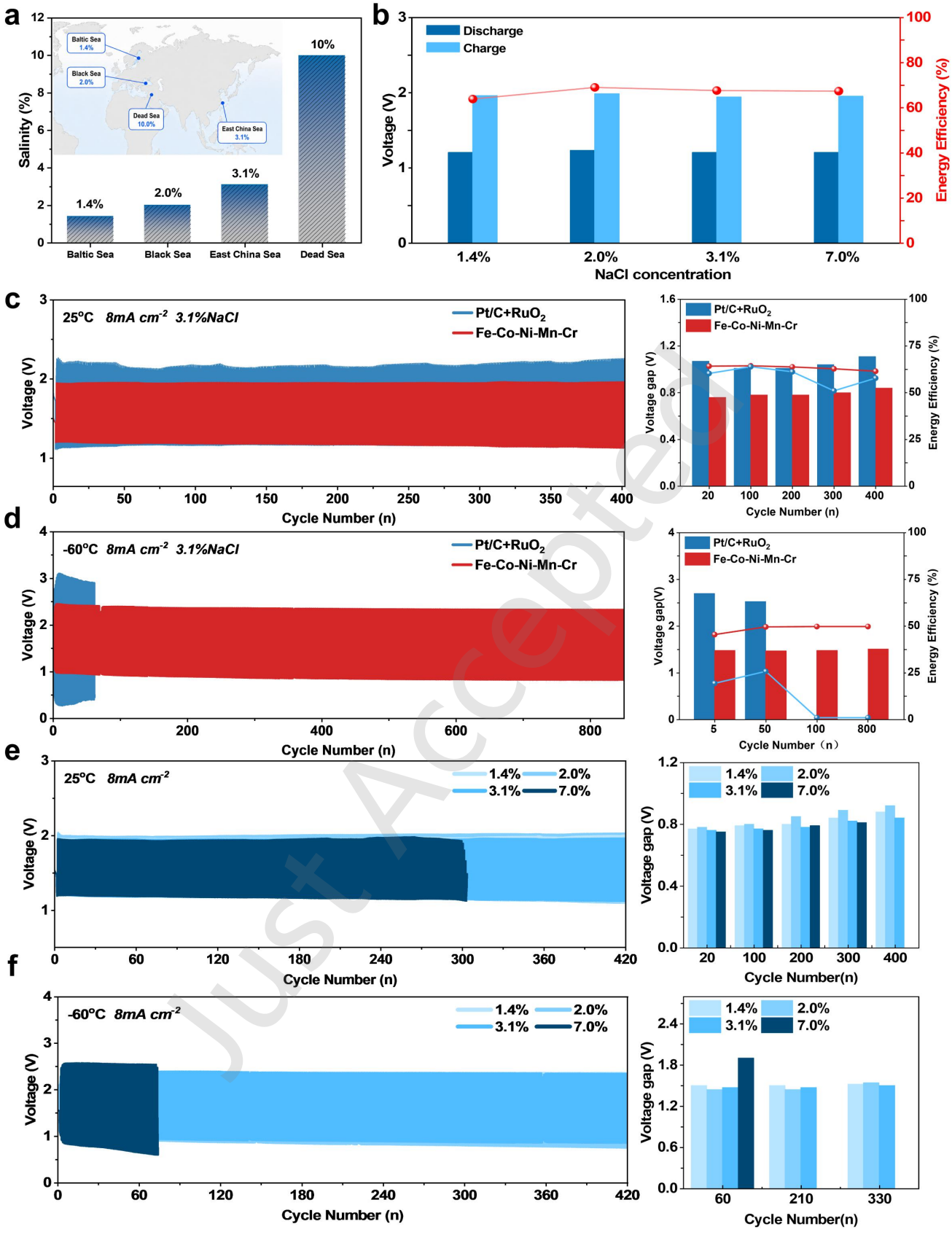


Figure 4. Salinity- and temperature-dependent cycling performance of seawater-mimetic hydrogel Zn–air batteries. (a) NaCl-equivalent salinity references for selected natural saline environments; these values are not intended to reproduce their full ionic compositions. (b) Average charge–discharge voltages and energy efficiencies at different NaCl concentrations. (c, d) Cycling performance, voltage gaps and energy efficiencies of Fe-Co-Ni-Mn-Cr- and Pt/C+RuO_2 -based batteries at 25 and −60 °C, respectively. (e, f) Cycling performance and voltage gaps at different NaCl concentrations at 25 and −60 °C, respectively.

2.4 *Cycling Stability and Salinity Adaptability*

We systematically investigated the influence of NaCl concentration on the electrochemical performance of Fe-Co-Ni-Mn-Cr-based zinc–air batteries (**Figure 4**). Controlled saline environments were established by introducing different amounts of NaCl into the KOH-containing hydrogel electrolyte. The representative salinities shown in Figure 4a are simplified NaCl-based references for selected natural saline environments and are

Just Accepted

not intended to reproduce their complete ionic compositions [9, 11]. For electrochemical evaluation, hydrogel electrolytes containing 1.4, 2.0, 3.1 and 7.0 wt% NaCl were prepared, and each composition was evaluated using an independently assembled battery under otherwise identical conditions. Although the salinity reference for the Dead Sea is approximately 10 wt% in Figure 4a, we selected 7.0 wt% NaCl as the highest electrochemically operable concentration, because higher values caused severe performance deterioration. The initial charge–discharge behaviour was evaluated at 25 °C and 8 mA cm^{-2} (Figure 4b). Averaged over the first ten cycles, the discharge voltages are 1.201, 1.230, 1.201 and 1.201 V for the electrolytes containing 1.4, 2.0, 3.1 and 7.0 wt% NaCl, respectively. The corresponding charge voltages are 1.959, 1.983, 1.940 and 1.950 V. All four electrolyte compositions therefore support reversible charge and discharge at room temperature, with only minor variations in their initial operating voltages. Because identical current densities and capacities were used for the charge and discharge steps, the energy efficiency was determined from the ratio of the discharge voltage to the charge voltage. The similar voltage profiles and energy efficiencies demonstrate that increasing the NaCl concentration to 7.0 wt% has a limited influence on the initial room-temperature response. The effects of salinity become evident primarily during prolonged cycling and low-temperature operation.

We selected the hydrogel containing 3.1 wt% NaCl as a representative seawater-mimetic electrolyte for comparison with the commercial catalyst benchmark (Figure 4c, d). At 25 °C and 8 mA cm^{-2}, the Fe-Co-Ni-Mn-Cr-based battery maintains well-defined charge and discharge plateaus over 400 cycles (Figure 4c). Throughout this period, its charge–discharge voltage gap remains smaller than that of the Pt/C+RuO_2 -based battery, resulting in correspondingly higher energy efficiency. The performance difference becomes substantially more pronounced at −60 °C (Figure 4d). Under this cryogenic condition, the Fe-Co-Ni-Mn-Cr-based battery retains reversible charge–discharge behavior for more than 800 cycles, whereas the Pt/C+RuO_2 -based battery exhibits severe voltage fluctuations and fails after approximately 50 cycles. These results demonstrate that the Fe-Co-Ni-Mn-Cr air cathode sustains a stable bifunctional oxygen-electrode response in the alkaline chloride-containing hydrogel, even when low temperature strongly restricts oxygen transport, ionic conduction and interfacial reaction kinetics. We further examined the salinity dependence of long-term cycling stability using independently assembled Fe-Co-Ni-Mn-Cr-based batteries (Figure 4e, f). At 25 °C, batteries containing 1.4, 2.0, 3.1 and 7.0 wt% NaCl achieve cycling lifetimes of 423, 782, 623 and 301 cycles, respectively (Figure 4e). Figure 4e displays only the first 420 cycles of these tests, so cells that survived beyond 420 cycles are truncated in the panel. At the 20th cycle, their voltage gaps remain similar, ranging from approximately 0.75 to 0.78 V, confirming that the initial polarization is relatively insensitive to NaCl concentration within the investigated range. With prolonged cycling, however, polarization develops gradually. At the 300th cycle, the voltage gaps increase to 0.84, 0.89, 0.82 and 0.81 V for the 1.4, 2.0, 3.1 and 7.0 wt% NaCl electrolytes, respectively. Although the 7.0 wt% NaCl battery exhibits a voltage gap comparable to those of the other batteries at this stage, it fails after approximately 301 cycles, whereas the batteries containing 1.4–3.1 wt% NaCl sustain substantially longer operation. These results indicate that moderate NaCl concentrations support prolonged room-temperature cycling, whereas excessive salinity compromises long-term stability through degradation processes that the initial voltage response does not fully reflect. The effect of NaCl concentration becomes considerably stronger at −60 °C (Figure 4f). The batteries containing 1.4, 2.0, 3.1 and 7.0 wt% NaCl exhibit cycling lifetimes of 863, 560, 1,992 and 68 cycles, respectively (Figure 4f displays the first 420 cycles of these tests), revealing a non-monotonic relationship between salinity and low-temperature durability. Among the tested compositions, the 3.1 wt% NaCl electrolyte provides the longest cycling life. At the 60th cycle, the voltage gaps of the batteries containing 1.4, 2.0 and 3.1 wt% NaCl are 1.50, 1.44 and 1.47 V, respectively. In comparison, the 7.0 wt% NaCl battery already exhibits a substantially larger voltage gap of 1.90 V. After 210 cycles, the voltage gaps of the 1.4–3.1 wt% batteries remain within 1.44–1.50 V and increase only moderately to 1.50–1.54 V by the 330th cycle. The 7.0 wt% battery, by contrast, loses reversible cycling after only 68 cycles. The exceptionally long cycling life achieved with the 3.1 wt% NaCl electrolyte suggests that an intermediate salinity provides a favorable balance among low-temperature electrolyte fluidity, ionic transport and electrode–electrolyte interfacial stability. By contrast, the rapid deterioration observed at 7.0 wt% NaCl may arise from stronger ion association, increased electrolyte viscosity, reduced ionic mobility and intensified chloride-related interfacial degradation. These limitations become particularly detrimental at −60 °C, where molecular transport and electrochemical reaction kinetics are already severely restricted. The results therefore reveal a pronounced temperature-dependent salinity effect: moderate NaCl concentrations support prolonged reversible operation, whereas excessive NaCl induces severe polarization and premature cell failure under cryogenic conditions.

Because the cycling stability of a full zinc–air battery is also influenced by the Zn-anode interface, Zn deposition morphology was examined ex situ after deposition in 8 M KOH at 2 mA cm^{-2} to an areal capacity of 20 mAh cm^{-2} over 10 h (Figure S8). At 25 °C, the deposited Zn exhibits a rough, loosely packed morphology composed of irregular plate-like and flower-like aggregates. In contrast, deposition at −60 °C produces finer, denser and more uniformly distributed Zn deposits, indicating that cooling substantially alters Zn nucleation and growth. The more homogeneous morphology formed at −60 °C may alleviate local current-density heterogeneity and thereby improve anode interfacial stability. However, because these experiments were performed in 8 M KOH without systematically varying the NaCl concentration, they primarily reveal the influence of temperature on Zn deposition and cannot alone explain the salinity-dependent cycling trend observed in Figure 4f.

Overall, the cycling behavior of the full battery arises from the coupled contributions of the air cathode, saline hydrogel electrolyte and Zn-anode interface. The multicomponent HEA provides diverse local adsorption environments for bifunctional oxygen electrocatalysis, while the nanoporous graphene shells and CNT channels limit direct exposure of the HEA nanoparticles without obstructing electron transport or reactant access. Concurrently, the hydrogel immobilizes the saline aqueous phase, and the temperature-dependent Zn deposition behavior contributes to anode interfacial stability. Together, these components enable reversible cycling within the tested

Not Accepted

salinity range and sustained operation at ultra-low temperatures, with 7.0 wt% NaCl serving as a high-salinity stress condition that leads to cell failure after 68 cycles at −60 °C.

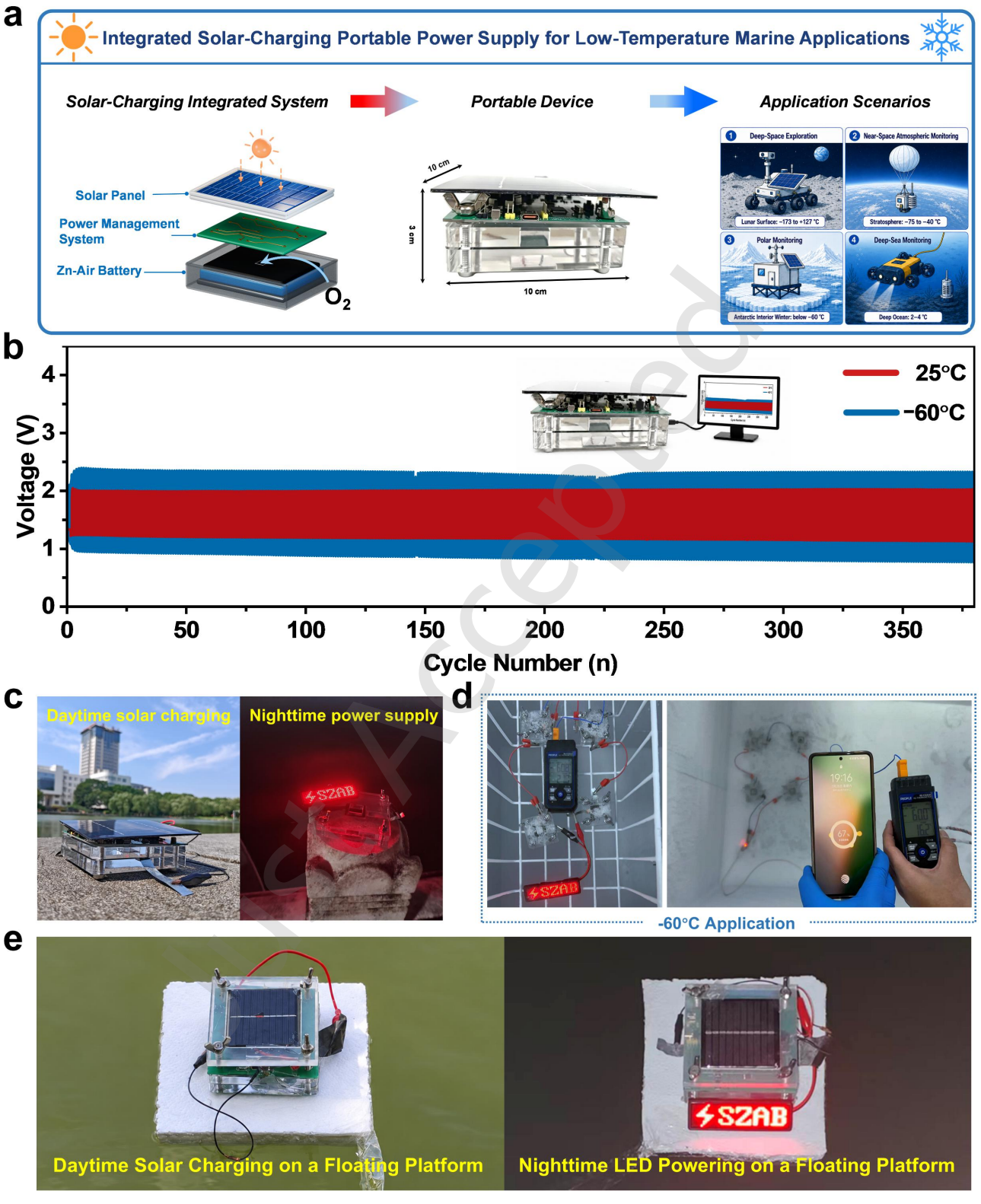


Figure 5. Integrated solar-rechargeable Zn–air battery system and practical demonstrations. (a) System configuration, portable device and representative application scenarios. (b) Charge–discharge cycling profiles at 25 and −60 °C. (c) Daytime solar charging and nighttime power supply. (d) LED powering and smartphone charging at −60 °C. (e) Daytime solar charging and nighttime LED powering on a floating platform.

2.5 *Integrated Solar-Rechargeable Portable Power Supply for Low-Temperature Marine Applications*

To extend the seawater-mimetic hydrogel zinc–air battery from cell-level evaluation to a practical device, we constructed a compact solar-rechargeable power-supply system based on the Fe-Co-Ni-Mn-Cr battery (**Figure 5**a). The system comprises a

solar panel, a power-management module and a zinc–air battery pack integrated into a portable device with approximate dimensions of 10 × 10 × 3 cm^3. The circuit board used in the power-management module is shown in Figure S9. Under illumination, the solar panel converts incident solar energy into electrical energy, while the power-management module regulates battery charging and subsequent power delivery. This configuration integrates energy harvesting, electrochemical storage and electrical output within a single portable platform. The representative scenarios in Figure 5a—including polar monitoring, near-space atmospheric observation, deep-sea monitoring and deep-space exploration—illustrate potential applications in remote or thermally demanding environments. The cycling performance of the integrated system was evaluated at 25 and −60 °C (Figure 5b). At a current density of 8 mA cm^{-2}, the device maintains reversible charge–discharge operation for more than 400 cycles at both temperatures, with well-defined voltage plateaus throughout the measurement. As expected, the charge–discharge voltage gap is larger at −60 °C than at 25 °C. This increased polarization is consistent with the reduced ionic conductivity of the hydrogel electrolyte, slower oxygen-electrode kinetics and higher interfacial resistance under cryogenic conditions. Nevertheless, the voltage profiles remain comparatively stable during prolonged cycling at −60 °C, confirming that the integrated system retains continuous electrochemical energy-storage capability under severe low-temperature conditions.

Solar-rechargeable operation was subsequently demonstrated under outdoor conditions (Figure 5c). During daytime illumination, the photovoltaic panel harvests solar energy and charges the zinc–air battery through the power-management module. After illumination is removed, the stored energy is released to power an LED load at night. This sequential demonstration completes the energy-conversion pathway from photovoltaic harvesting to electrochemical storage and subsequent electrical output, establishing the zinc–air battery as a functional energy-storage component in an integrated solar-powered system. The practical low-temperature output of the battery system was further examined at −60 °C (Figure 5d). Under this condition, the battery successfully powers an LED array and supplies electrical energy to a commercial smartphone. These demonstrations provide direct evidence that useful electrical output is retained under ultra-low-temperature conditions, beyond electrochemical testing with laboratory instrumentation. Because the LED and smartphone experiments are functional demonstrations rather than calibrated load measurements, we infer no quantitative power or energy-delivery values from the photographs. To explore its suitability for water-surface applications, we mounted the integrated device on a floating platform and tested it on a freshwater lake (Figure 5e). The system remained operational while floating, demonstrating mechanical integration and electrical functionality in a water-surface environment. Importantly, the lake water served only as the external testing environment; the battery continued to operate using its internally contained NaCl-containing seawater-mimetic hydrogel electrolyte. The experiment should therefore be interpreted as a device-level floating demonstration rather than direct utilization of natural lake water as the battery electrolyte.

Collectively, the integrated platform combines solar-energy harvesting, rechargeable electrochemical storage and practical electrical output within a compact portable device. Its stable charge–discharge operation at −60 °C, ability to power representative electronic loads under cryogenic conditions, and compatibility with a floating deployment platform extend the Fe-Co-Ni-Mn-Cr-based zinc–air battery from laboratory-scale electrochemical evaluation toward integrated power supplies for remote, low-temperature, and water-surface application.

3 Conclusions

We developed a hierarchically nanoconfined Fe-Co-Ni-Mn-Cr HEA catalyst for salinity-tolerant seawater-mimetic hydrogel ZABs. Few-layer porous graphene shells and CNT channels provide complementary confinement of the HEA nanoparticles while retaining electron- and O_2 /OH^- -transport pathways. The catalyst exhibits bifunctional oxygen electrocatalytic activity, and the resulting battery delivers a peak power density of 407.82 mW cm^{-2} at 25 °C and sustains reversible cycling for more than 800 cycles at −60 °C and 8 mA cm^{-2} in 8 M KOH + 3.1 wt% NaCl. Batteries with 1.4–3.1 wt% NaCl remain reversible at −60 °C, whereas the 7.0 wt% NaCl cell is a high-salinity stress condition that fails after 68 cycles. A photovoltaic-coupled pack further powers an LED array and charges a smartphone at −60 °C. Hierarchical catalyst confinement combined with a saline hydrogel electrolyte therefore enables ZAB operation under coupled salinity variation and ultra-low temperature.

Electronic Supplementary Material: Supplementary material (Figures S1–S9) is available in the online version of this article at https://doi.org/10.26599/NR.2026.94909316.

Data availability

The data that support the findings of this study are available from the corresponding author upon reasonable request.

Declaration of competing interest

All the contributing authors report no conflict of interests in this work.

Author contribution statement

H.C. Song: Writing–review & editing, Visualization, Formal analysis, Resources, Conceptualization, Project administration. Y.X. Liu: Writing–original draft, Data curation, Software, Formal analysis, Methodology, Validation. D.E. Li and X.L. Ding: Data curation, Methodology, Investigation. M. Wang and Y.Z. Zhang: Methodology, Formal analysis. C.S. Wang: Validation, Formal analysis. J. Wu: Formal analysis, Conceptualization. G.B. Zhang: Investigation, Supervision. J. Xu: Supervision, Resources, Project administration, Funding acquisition, Conceptualization.

Use of AI statement

Acknowledgements

This research was partially supported by the National Natural Science Foundation of China (Grant Nos. 61921005, 62474160, 61735008, 62104099 and 62004078) and the Key R&D Project of Nantong (No. 2024004).

Just Accepted

During the preparation of this work, the authors used ChatGPT (OpenAI) in order to adjust the viewing angle of the two photographs shown in Figure 5e and the brightness of the water surface in these photographs. After using this tool/service, the authors reviewed and edited the content as needed and take full responsibility for the content of the publication.

References

[1] Shang, Y.;Huang, Y.;Li, L.;Wu, F.;Chen, R. Electrochemical energy storage toward extreme conditions: driving human exploration beyond current boundaries. *Chem. Rev.* **2025**, *125*, 5674-5744.

[2] Wang, C.;Zhou, S.;Shu, X.;Song, H. Deep-sea mining: a potential solution to secure critical energy minerals availability. *npj Ocean Sustainability*. **2025**, *4*, 59.

[3] Chen, M.;Zhang, Y.;Xing, G.;Chou, S.;Tang, Y. Electrochemical energy storage devices working in extreme conditions. *Energy Environ. Sci.* **2021**, *14*, 3323-3351.

[4] Gu, T.;Jia, Y.;Zhang, L.;Zhao, L.;Shen, J.;Ouyang, L.;Zhu, M.;Liu, J. Ampere-hour-scale quasi-solid-state zinc-air batteries with a wide operating temperature range (-50 to 60 °C). *J. Am. Chem. Soc.* **2025**, *147*, 15029-15040.

[5] Han, Y.;Zhao, Y.;Yu, Y. Research progress of zn-air batteries suitable for extreme temperatures. *Energy Storage Mater.* **2024**, *69*, 103429.

[6] Wang, Q.;Feng, Q.;Lei, Y.;Tang, S.;Xu, L.;Xiong, Y.;Fang, G.;Wang, Y.;Yang, P.;Liu, J. et al. Quasi-solid-state zn-air batteries with an atomically dispersed cobalt electrocatalyst and organohydrogel electrolyte. *Nat. Commun.* **2022**, *13*, 3689.

[7] Ruppert, J.;Stegemann, L.;Bauer, A.;Bieker, P.;Grünebaum, M.;Tempel, H.;Windmüller, A.;Leker, J.;Winter, M.;Eichel, R.-A. et al. Competitive rechargeable zinc batteries for energy storage. *Adv. Energy Mater.* **2025**, *15*, e02866.

[8] Shinohara, M.;Araki, E.;Mochizuki, M.;Kanazawa, T.;Suyehiro, K. Practical application of a sea-water battery in deep-sea basin and its performance. *J. Power Sources*. **2009**, *187*, 253-260.

[9] Yu, J.;Li, B.-Q.;Zhao, C.-X.;Zhang, Q. Seawater electrolyte-based metal-air batteries: from strategies to applications. *Energy Environ. Sci.* **2020**, *13*, 3253-3268.

[10] Li, Y.;Dai, H. Recent advances in zinc–air batteries. *Chem. Soc. Rev.* **2014**, *43*, 5257-5275.

[11] Yu, J.;Zhao, C.-X.;Liu, J.-N.;Li, B.-Q.;Tang, C.;Zhang, Q. Seawater-based electrolyte for zinc–air batteries. *Green Chem. Eng.* **2020**, *1*, 117-123.

[12] Zhao, C.-X.;Zhang, Q. Zinc–air batteries can fulfill diversified application scenarios. *InfoScience*. **2024**, *1*, e12014.

[13] Wu, M.;Huang, N.;Lv, M.;Wang, F.;Ma, F.;Deng, Y.;Sun, P.;Zheng, Y.;Liu, W.;Ye, L. Organic-inorganic hybrid hydrogel electrolyte for high-performance quasi-solid-state zinc-air batteries. *Front. Chem. Sci. Eng.* **2025**, *19*, 15.

[14] Zhang, T.;Wu, N.;Zhao, Y.;Zhang, X.;Wu, J.;Weng, J.;Li, S.;Huo, F.;Huang, W. Frontiers and Structural Engineering for Building Flexible Zinc–Air Batteries. *Adv. Sci.* **2022**, *9*, 2103954.

[15] Cao, Z.;Hu, H.;Wu, M.;Tang, K.;Jiang, T. Planar all-solid-state rechargeable zn–air batteries for compact wearable energy storage. *J. Mater. Chem. A*. **2019**, *7*, 17581-17593.

[16] Chen, S.;Wang, T.;Ma, L.;Zhou, B.;Wu, J.;Zhu, D.;Li, Y. Y.;Fan, J.;Zhi, C. Aqueous rechargeable zinc air batteries operated at −110°C. *Chem*. **2023**, *9*, 497-510.

[17] Santos, F.;Tafur, J. P.;Abad, J.;Fernández Romero, A. J. Structural modifications and ionic transport of PVA-KOH hydrogels applied in zn/air batteries. *J. Electroanal. Chem.* **2019**, *850*, 113380.

[18] Wu, J.;Wang, Y.;Deng, D.;Bai, Y.;Liu, M.;Zhao, X.;Xiong, X.;Lei, Y. Low-temperature resistant gel polymer electrolytes for zinc–air batteries. *J. Mater. Chem. A*. **2022**, *10*, 19304-19319.

[19] Zhang, T.;Wang, K.;Chen, Y.;Liu, H.;Wang, H.;Wei, M.;Zhao, J.;Long, Q.;Pei, P. A water-anchored hydrogel with high water retention for wide-temperature zinc-air batteries. *Chem. Eng. J.* **2026**, *546*, 180136.

[20] Pei, Z.;Yuan, Z.;Wang, C.;Zhao, S.;Fei, J.;Wei, L.;Chen, J.;Wang, C.;Qi, R.;Liu, Z.;Chen, Y. A flexible rechargeable zinc–air battery with excellent low-temperature adaptability. *Angew. Chem. Int. Ed.* **2020**, *59*, 4793-4799.

[21] Zhang, Y.;Qin, H.;Mensah, A.;Ke, H.;Cai, Y.;Wang, Q.;Huang, F.;Liu, B.;Lv, P. F.;Wei, Q. F. Reaction modifier system enable double-network hydrogel electrolyte for flexible zinc-air batteries with tolerance to extreme cold conditions. *Energy Storage Mater.* **2021**, *42*, 88-96.

[22] Zhong, X.;Zheng, Z.;Xu, J.;Xiao, X.;Sun, C.;Zhang, M.;Ma, J.;Xu, B.;Yu, K.;Zhang, X. et al. Flexible zinc–air batteries with ampere-hour capacities and wide-temperature adaptabilities. *Adv. Mater.* **2023**, *35*, 2209980.

[23] Hopkins, B. J.;Chervin, C. N.;Parker, J. F.;Long, J. W.;Rolison, D. R. Electrocatalyst or support? Circumventing corrosion for long-lived zinc–air batteries. *Next Energy*. **2023**, *1*, 100054.

[24] Tang, W.;Mai, J.;Liu, L.;Yu, N.;Fu, L.;Chen, Y.;Liu, Y.;Wu, Y.;Van Ree, T. Recent advances of bifunctional catalysts for zinc air batteries with stability considerations: from selecting materials to reconstruction. *Nanoscale Adv.* **2023**, *5*, 4368-4401.

[25] Wang, T.;Shi, Z.;Wang, F.;He, J.;Zhong, Y.;Ma, Y.;Zhu, Z.;Cheng, X.-B.;Ozoemena, K. I.;Wu, Y. Advanced bifunctional catalyst design for rechargeable zinc–air batteries. *EES Catalysis*. **2024**, *2*, 696-726.

[26] Liu, H.;Liu, Q.;Wang, Y.;Wang, Y.;Chou, S.;Hu, Z.;Zhang, Z. Bifunctional carbon-based cathode catalysts for zinc-air battery: A review. *Chin. Chem. Lett.* **2022**, *33*, 683-692.

[27] Gao, Y.;Liu, L.;Jiang, Y.;Yu, D.;Zheng, X.;Wang, J.;Liu, J.;Luo, D.;Zhang, Y.;Shi, Z. et al. Design principles and mechanistic understandings of non-noble-metal bifunctional electrocatalysts for Zinc–air batteries. *Nano-Micro Lett.* **2024**, *16*, 162.

[28] Kim, J.;Lee, J.;Kim, S.;Jung, W. Improved catalytic properties of fluorine-doped $La_{0.6}Sr_{0.4}Co_{0.2}Fe_{0.8}O_3$-delta for air electrode with high-performance metal-air batteries. *Electron. Mater. Lett.* **2024**, *20*, 450-458.

[29] Chang, H.;Shi, L.-N.;Chen, Y.-H.;Wang, P.-F.;Yi, T.-F. Advanced MOF-derived carbon-based non-noble metal oxygen electrocatalyst for next-generation rechargeable zn-air batteries. *Coord. Chem. Rev.* **2022**, *473*, 214839.

[30] Batchelor, T. a. A.;Pedersen, J. K.;Winther, S. H.;Castelli, I. E.;Jacobsen, K. W.;Rossmeisl, J. High-entropy alloys as a discovery platform for electrocatalysis. *Joule*. **2019**, *3*, 834-845.

[31] Glasscott, M. W.;Pendergast, A. D.;Goines, S.;Bishop, A. R.;Hoang, A. T.;Renault, C.;Dick, J. E. Electrosynthesis of high-entropy metallic glass nanoparticles for designer, multi-functional electrocatalysis. *Nat. Commun.* **2019**, *10*, 2650.

[32] He, R.;Yang, L.;Zhang, Y.;Wang, X.;Lee, S.;Zhang, T.;Li, L.;Liang, Z.;Chen, J.;Li, J. et al. A CrMnFeCoNi high entropy alloy boosting oxygen evolution/reduction reactions and zinc-air battery performance. *Energy Storage Mater.* **2023**, *58*, 287-298.

[33] Yen, F.-Y.;Chang, S.-I.;Ting, Y.-C.;Chang, C.-W.;Lee, K.-A.;Lu, S.-Y. In-situ selective oxidation created Cr_2O_3 assisting CrMnFeCoNi for ultrahigh power density zinc-air batteries. *Energy Materials*. **2025**, *5*, 500114.

[34] Xia, L.;Dai, P.;Huang, K.;Zhang, H.;Peng, Z.;Wu, M. Thermally tuning FeCoNiCrMn high-entropy alloy in carbon nanofibers for superior bifunctional oxygen electrocatalysis toward flexible zinc-air batteries. *Dalton transactions*. **2026**, *55*, 7566-7576.

Just Accepted

[35] Qiu, H.-J.;Fang, G.;Gao, J.;Wen, Y.;Lv, J.;Li, H.;Xie, G.;Liu, X.;Sun, S. Noble metal-free nanoporous high-entropy alloys as highly efficient electrocatalysts for oxygen evolution reaction. *ACS Mater. Lett.* **2019**, *1*, 526-533.

[36] Luan, C.;Escalera-López, D.;Hagemann, U.;Kostka, A.;Laplanche, G.;Wu, D.;Cherevko, S.;Li, T. Revealing dynamic surface and subsurface reconstruction of high-entropy alloy electrocatalysts during the oxygen evolution reaction at the atomic scale. *ACS Catal.* **2024**, *14*, 12704-12716.

[37] Li, W.;Wang, Y.;Sun, X.;Dong, H.;Sun, L.;Zhang, X.;Li, Y. High-entropy spinel oxides with oxygen-rich vacancies improve the catalytic performance for low-temperature flexible zinc-air batteries. *ACS Sustain. Chem. Eng.* **2025**, *13*, 16459-16473.

[38] Qiu, Z.;Guo, X.;Cao, S.;Du, M.;Wang, Q.;Pi, Y.;Pang, H. High-entropy Ag-Ru-based electrocatalysts with dual-active-center for highly stable ultra-low-temperature zinc-air batteries. *Angew. Chem. Int. Ed.* **2025**, *64*, e202415216.

[39] Deng, J.;Ren, P.;Deng, D.;Bao, X. Enhanced electron penetration through an ultrathin graphene layer for highly efficient catalysis of the hydrogen evolution reaction. *Angew. Chem. Int. Ed.* **2015**, *54*, 2100-2104.

[40] Najam, T.;Shah, S. S. A.;Ding, W.;Ling, Z.;Li, L.;Wei, Z. Electron penetration from metal core to metal species attached skin in nitrogen-doped core-shell catalyst for enhancing oxygen evolution reaction. *Electrochim. Acta*. **2019**, *327*, 134939.

[41] Liu, X.;Li, L.;Li, Z.;Xu, H.;Zhao, Z.;Li, Y.;Gao, Y.;Xu, X.;Wu, H. Boosting bifunctional oxygen electrocatalysis via FeCoNiCuMn high-entropy alloy encapsulated within N-doped carbon core-shell structures for high-performance zinc-air batteries. *ChemSusChem*. **2026**, *19*, e70742.

[42] Miao, W.;Cao, X.;Qin, M.;Lv, E.;Yu, H.;Zhang, X.;Dong, X. N-doping FeNi@C(N_x) core-shell nanoparticles synthesized by arc plasma as a highly efficient bifunctional electrocatalyst for all-solid zinc-air batteries. *Composites Part B: Engineering*. **2023**, *260*, 110769.

[43] Wang, Y.;Zhang, C.;Wang, X.;Duan, J.;Tong, K.;Dai, S.;Chu, L.;Huang, M. Engineering carbon-chainmail-shell coated Co_9Se_8 nanoparticles as efficient and durable catalysts in seawater-based zn-air batteries. *Acta Physico-Chimica Sinica*. **2024**, *40*, 2305004.

[44] Lu, Q.;Zou, X.;Bu, Y.;Shao, Z. Structural design of supported electrocatalysts for rechargeable zn-air batteries. *Energy Storage Mater.* **2023**, *55*, 166-192.

[45] Kogler, M.;Olgiati, M.;Ostermann, M.;Rachle, P.;Gahlawat, S.;Valtiner, M.;Pichler, C. M. Bulk-independent surface oxide composition controls the electrochemical performance of high-entropy alloys. *J. Mater. Chem. A*. **2024**, *12*, 22565-22575.

[46] Liu, Y.;Feng, S.;Shan, L.;Zhu, Y.;Zhou, C.;Li, J.;Shi, X.;Kang, Z.;Tian, X.;Rao, P. Localized negatively charged interfaces for seawater electrolyte - based zinc - air batteries. *Adv. Funct. Mater.* **2025**, *35*, 2422874.

[47] Liu, Y.-R.;Zhang, M.;Yu, Y.-H.;Liu, Y.-L.;Li, J.;Shi, X.-D.;Kang, Z.-Y.;Wu, D.-X.;Rao, P.;Liang, Y. Local electric fields coupled with Cl^- fixation strategy for improving seawater oxygen reduction reaction performance. *J. Electrochem.* **2025**, *31*, 2504132.

[48] Qiao, L.;Wang, X.;Xu, R.;Zhang, C.;Chen, K.;Tong, K.;Wang, H.;Dai, S.;Chu, L.;Huang, M. Nitrogen-doped carbon shell armored 'Janus' Co/Co_9S_8 heterojunction as robust bi-functional oxygen reduction reaction/oxygen evolution reaction catalysts in seawater-based rechargeable zn-air batteries. *Mater. Today Energy*. **2023**, *37*, 101398.

[49] Chen, X.;Zheng, X.;Yin, Z.;Lu, J.;Wang, Y.;Guo, Y.;Zhang, J.;Wang, H.;Zhao, Z.;Wu, Y.;Deng, Y. Pre-adsorption of chlorine enhances the oxyphilic property and oxygen reduction activity of Fe/Se-NC electrocatalyst in seawater electrolyte. *Chem. Eng. J.* **2024**, *482*, 148856.

[50] Liu, Y.;Zhu, Y.;Zhang, Y.;Rao, P.;Li, J.;Shan, L.;Tang, B.;Shi, X.;Kang, Z.;Tian, X. Pyridine nitrogen decorated carbon support for high-performance seawater electrolyte-based zinc-air battery. *Angew. Chem. Int. Ed.* **2025**, *64*, e202509911.

[51] Hao, M.-D.;Li, Q.;Sun, J.-H.;Liu, D.;Yu, H.-L.;Liu, R. Polyphenol-metal coordination derived high-entropy alloy as bifunctional oxygen electrocatalyst for zn-air batteries. *Rare Metals*. **2025**, *44*, 2836-2844.

© The Author(s) 20xx. *Nano Research* published by Tsinghua University Press. The articles published in this open access journal are distributed under the terms of the Creative Commons Attribution 4.0 International License (http://creativecommons.org/licenses/by/4.0/), which permits use, distribution and reproduction in any medium, provided the original work is properly cited.

Just Accepted

Electronic Supplementary Material

Ultra-low-temperature seawater zinc–air batteries enabled by carbon nanochannel-confined high-entropy alloy catalysts

Hucheng Song [1], Yixin Liu [1], Deen Li [1], Xilei Ding [1], Min Wang [2], Yuzi Zhang [1], Changshun Wang [1], Jing Wu [1], Guangbin Zhang [1], Jun Xu [2,3]

[1] School of Physics, Nanjing University of Aeronautics and Astronautics, Nanjing 211106, China
[2] School of Electronics Science and Engineering, National Laboratory of Solid State Microstructures, Nanjing University, Nanjing 210093, China
[3] School of Microelectronics, School of Physics, Nantong University 226019, China

Supporting information to https://doi.org/10.26599/NR.2026.94909316

Just Accepted

Address correspondence to Hucheng Song, hcsong@nuaa.edu.cn; Changshun Wang, changshun@nuaa.edu.cn; Jing Wu,

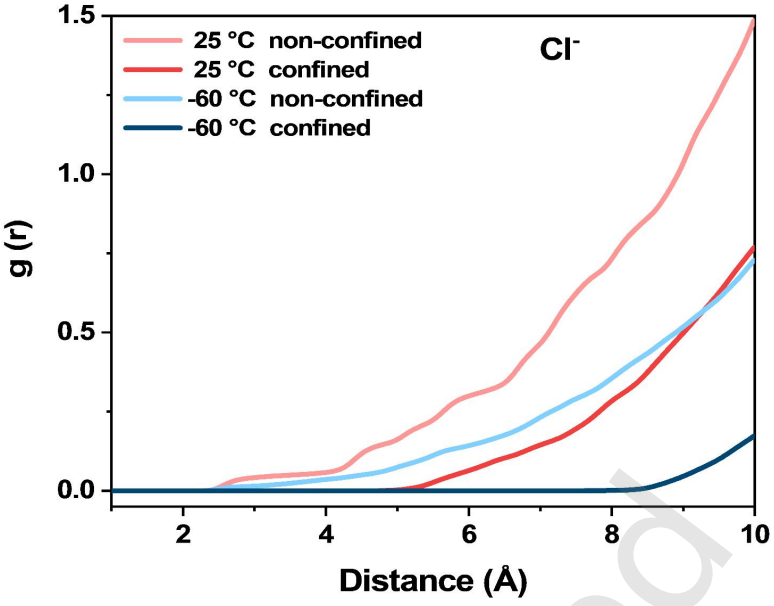


Figure S1. Radial distribution functions g(r) of Cl^- around the HEA surface for the confined and non-confined models at 25 and −60 °C. The reference group comprises the 392 metal atoms of the HEA; the cut-off distance is 10 Å. Each simulation cell contains 7 Na^+ and 7 Cl^- ions, and the statistics were collected over 4,801 frames (20–500 ps) after equilibration. The RDF is normalized to the bulk Cl^- density; because the confined geometry reduces the accessible volume, the curves are interpreted as a reduced probability of Cl^- encountering the HEA surface rather than as a thermodynamic exclusion coefficient.

Just Accepted

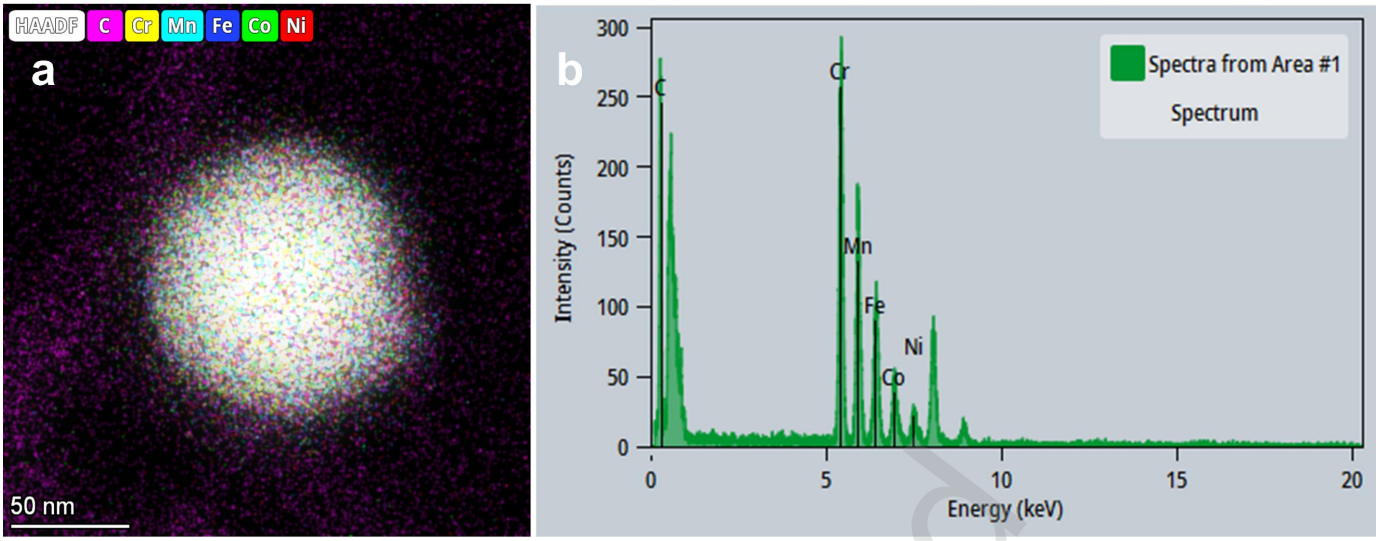


Figure S2. HAADF-TEM elemental mapping and EDS analysis of the Fe-Co-Ni-Mn-Cr catalyst. (a) Overlaid elemental maps of C, Cr, Mn, Fe, Co, and Ni, showing highly overlapped and uniformly distributed metal elements within the nanoparticle region. (b) EDS spectrum acquired from the selected region, revealing characteristic peaks of C, Cr, Mn, Fe, Co, and Ni.

The spatial elemental distribution and chemical composition of the Fe-Co-Ni-Mn-Cr catalyst were characterized by high-angle annular dark-field transmission electron microscopy (HAADF-TEM) combined with energy-dispersive X-ray spectroscopy. Figure S2a presents the overlaid elemental maps of C, Cr, Mn, Fe, Co, and Ni. The signals of Cr, Mn, Fe, Co, and Ni are highly overlapped and uniformly distributed within the nanoparticle region, with no observable elemental segregation or phase separation, indicating that these multi-principal elements form a homogeneous solid-solution structure, i.e., a single-phase high-entropy alloy. Meanwhile, the C signal is broadly distributed around the particle and in the surrounding region, consistent with the graphene shell encapsulating the alloy and the outer CNT/graphene conductive framework. The EDS spectrum acquired from the selected region (Figure S2b) clearly reveals characteristic peaks of C, Cr, Mn, Fe, Co, and Ni, with all metal elements exhibiting significant characteristic signals, further confirming that the chemical composition matches the expected Fe-Co-Ni-Mn-Cr quinary alloy system. Collectively, the elemental mapping and EDS results provide strong evidence for the successful construction of Fe-Co-Ni-Mn-Cr HEA nanoparticles within the carbon-confined framework.

Just Accepted

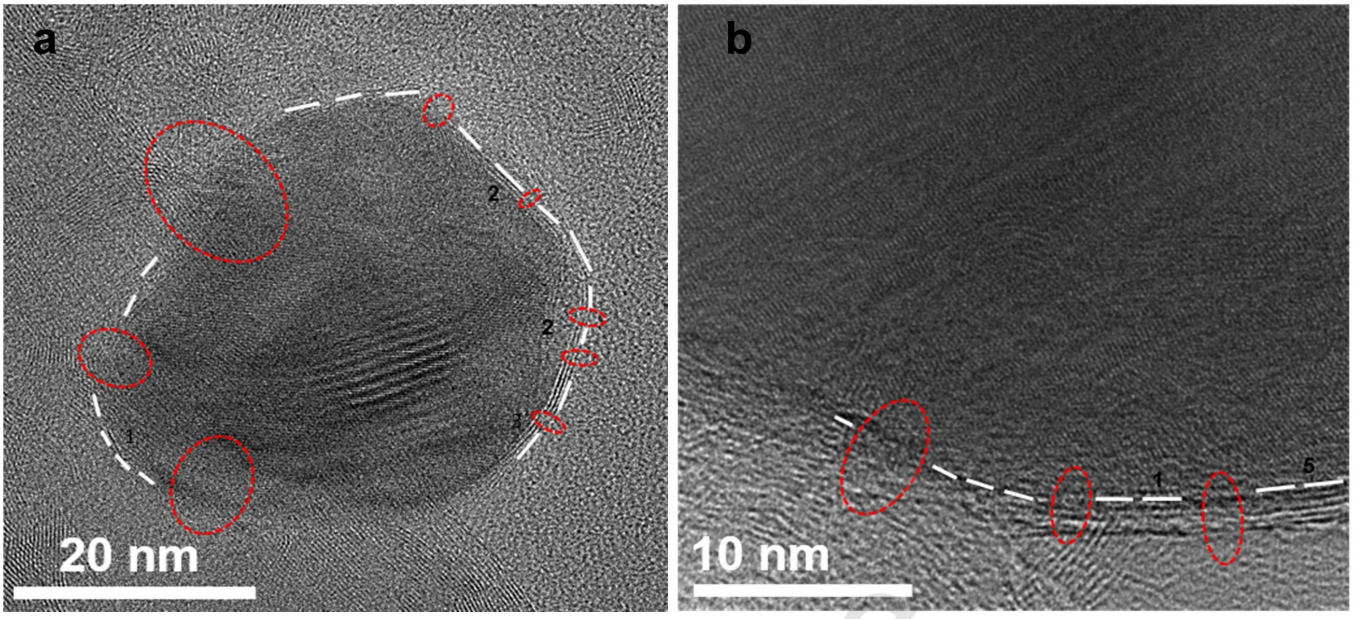


Figure S3. Graphene shell structure and nanoscale pore/opening analysis of Fe-Co-Ni-Mn-Cr nanoparticles. (a,b) TEM/HRTEM images showing the number of graphene stacking layers on the particle surface and the size distribution of nanoscale pores/openings.

The graphene shell surrounding the Fe-Co-Ni-Mn-Cr HEA nanoparticles is delineated by white dashed lines, forming a semi-wrapped confined structure on the particle surface. Nanoscale channels or openings in the graphene shell are marked by red circles. These channels connect the external electrolyte with the HEA/graphene interfacial region, allowing O_2 and OH^- to access the catalyst surface during oxygen electrode reactions. Meanwhile, the graphene shell confines the local interfacial region and reduces direct exposure of the HEA core to the alkaline electrolyte. Consequently, this semi-wrapped graphene shell structure simultaneously provides interfacial protection and accessible mass-transport pathways.

Just Accepted

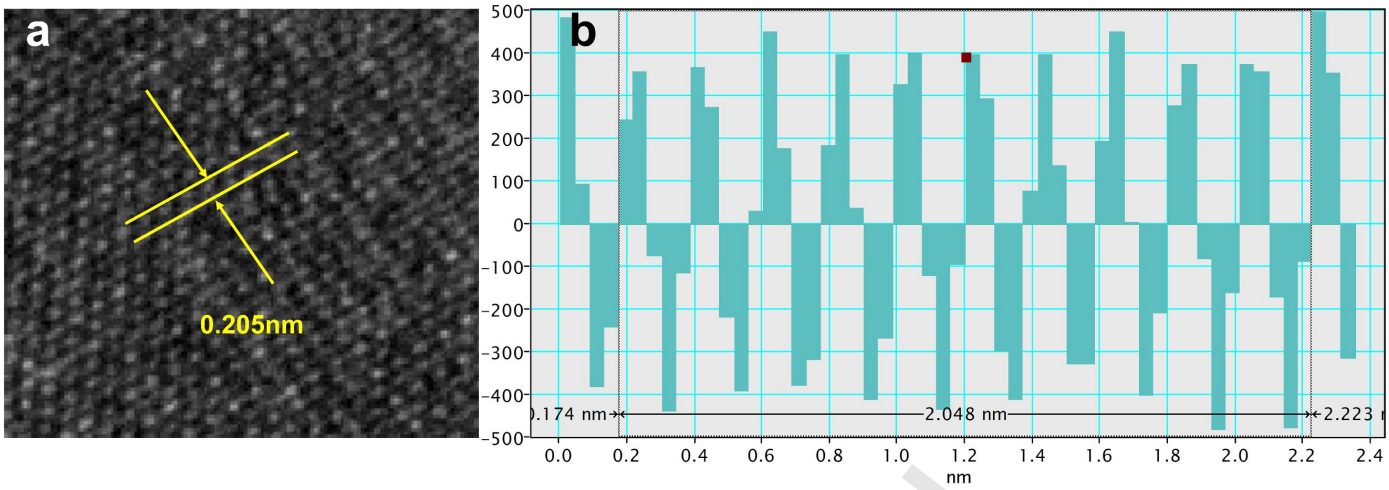


Figure S4. HRTEM image and line-profile intensity analysis of the Fe-Co-Ni-Mn-Cr HEA core. (a) HRTEM image of the alloy core with adjacent lattice planes marked by yellow parallel lines. (b) Corresponding line-profile intensity analysis, revealing a lattice spacing of approximately 0.205 nm, assigned to the (111) plane of the HEA phase.

The crystalline structure of the Fe-Co-Ni-Mn-Cr HEA core was characterized by high-resolution transmission electron microscopy. Figure S4a reveals clear and continuous lattice fringes within the HEA nanoparticle core, indicating excellent crystallinity. Adjacent lattice planes in the selected crystalline region are marked by yellow parallel lines. The corresponding line-profile intensity analysis (Figure S4b) exhibits periodic intensity oscillations arising from the repeated lattice fringes. The measured distance between the marked positions is approximately 2.048 nm, covering about 10 adjacent lattice spacings, yielding an average lattice spacing of approximately 0.205 nm, which is consistent with the (111) plane of the Fe-Co-Ni-Mn-Cr HEA phase in the fcc structure. This result not only confirms the crystalline integrity of the HEA core but also provides robust evidence for the successful alloying of the multi-component alloy nanoparticles during the rapid Joule heating process.

Just Accepted

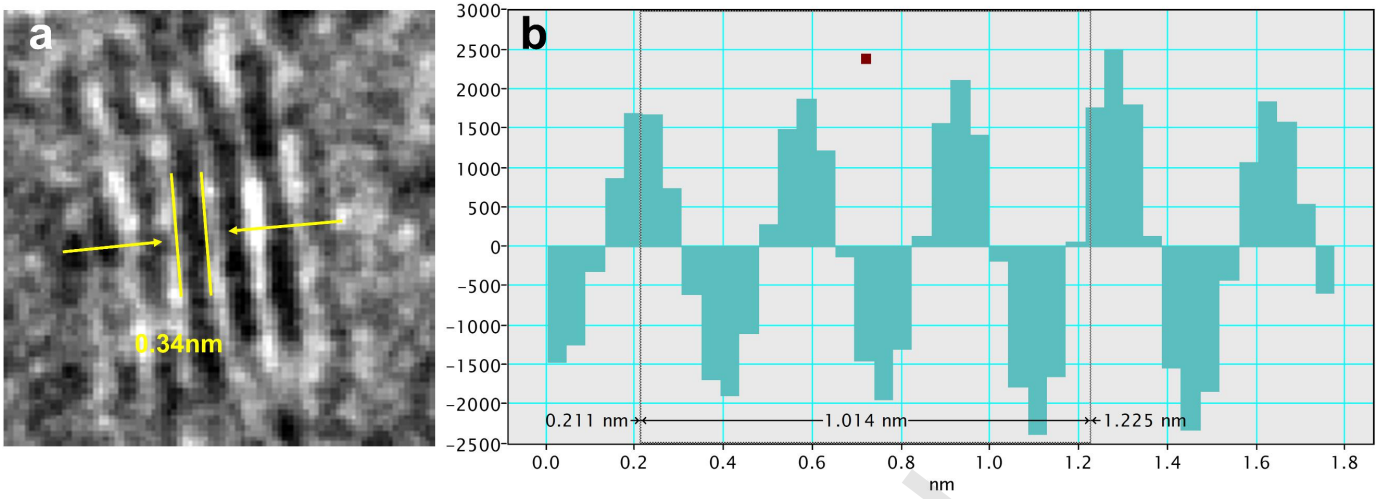


Figure S5. HRTEM image and line-profile intensity analysis of the graphene shell on Fe-Co-Ni-Mn-Cr HEA nanoparticles. (a) HRTEM image of the graphene shell region with adjacent graphitic layers marked by yellow parallel lines. (b) Corresponding line-profile intensity analysis, revealing an interlayer spacing of approximately 0.34 nm, assigned to the (002) plane of graphitic carbon.

The graphene shell encapsulating the Fe-Co-Ni-Mn-Cr HEA nanoparticles was characterized by high-resolution transmission electron microscopy. Figure S5a reveals clear and parallel lattice fringes within the graphene shell region surrounding the alloy nanoparticles, indicating a well-graphitized structure, with a measured single-layer spacing of approximately 0.34 nm. The corresponding line-profile intensity analysis (Figure S5b) exhibits periodic intensity oscillations arising from the repeated stacking of graphene layers. The measured distance between the marked positions is approximately 1.014 nm, covering three adjacent interlayer spacings, yielding an average interlayer spacing of approximately 0.34 nm, which is consistent with the (002) plane spacing of graphitic carbon/graphene. This result confirms the successful formation of a graphene shell around the HEA nanoparticles, a confined structure that is essential for protecting the inner alloy from corrosion in the alkaline electrolyte.

Just Accepted

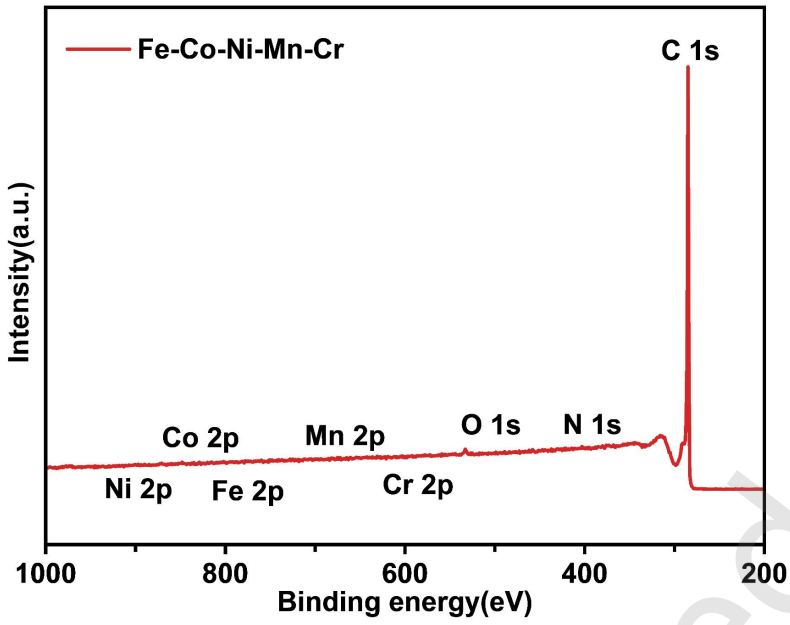


Figure S6. XPS survey spectrum of the Fe-Co-Ni-Mn-Cr catalyst, showing characteristic signals of C 1s, O 1s, N 1s, and Cr 2p, Mn 2p, Fe 2p, Co 2p, and Ni 2p.

The surface chemical composition of the Fe-Co-Ni-Mn-Cr catalyst was characterized by X-ray photoelectron spectroscopy. The survey spectrum (Figure S6) reveals clearly detectable characteristic signals of C 1s, O 1s, N 1s, and Cr 2p, Mn 2p, Fe 2p, Co 2p, and Ni 2p. The intense C 1s peak primarily originates from the CNT/graphene conductive framework and the graphene shell encapsulating the alloy, while the O 1s signal and the weak N 1s signal correspond to surface oxygen-containing functional groups/adsorbed oxygen species and trace nitrogen-containing species, respectively. Notably, although the characteristic peaks of all five metal elements (Cr, Mn, Fe, Co, and Ni) are identifiable, confirming the presence of multi-principal components on the catalyst surface, their relative intensities are relatively low. This is mainly because XPS is inherently sensitive to the topmost surface layer (typically <10 nm), and the Fe-Co-Ni-Mn-Cr HEA nanoparticles are partially covered by the outer graphene shell, resulting in attenuation of the metal signals. In combination with the EDS and elemental mapping results, the XPS analysis further confirms the coexistence and successful construction of the multi-metal Fe-Co-Ni-Mn-Cr components within the CNT/graphene-confined catalytic system.

Just Accepted

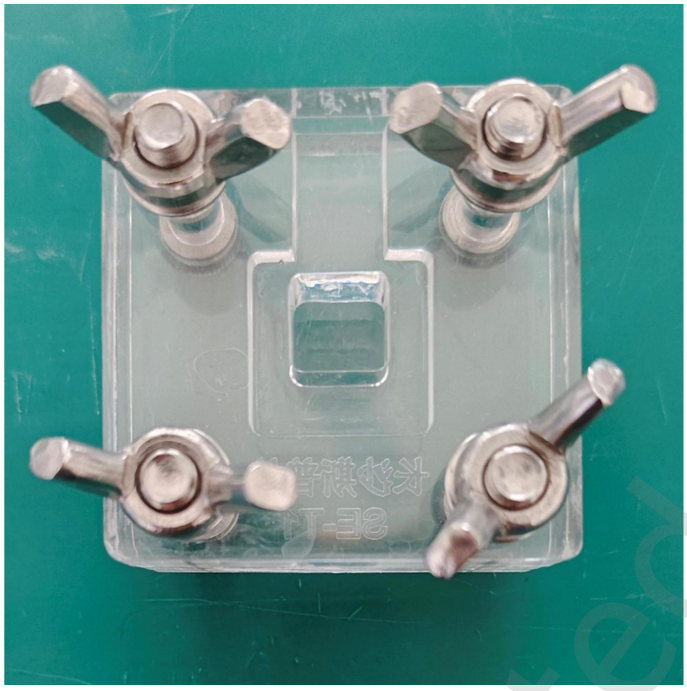


Figure S7. Photograph of the customized mold used for assembling flexible solid-state Zn–air batteries.

Just Accepted

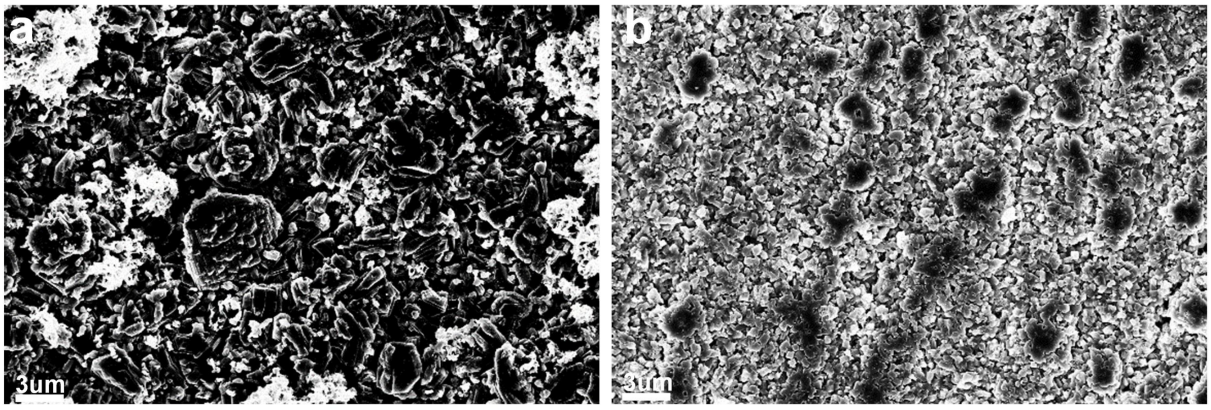


Figure S8. SEM comparison of Zn deposition morphologies at different temperatures. (a) Zn deposition morphology at 25 °C, showing a rough and loose structure with irregular plate-like/flower-like crystal stacks. (b) Zn deposition morphology at −60 °C, showing a smooth and dense fine-grained "cobblestone" structure.

The morphologies of Zn deposits formed at room temperature and ultra-low temperature were compared by scanning electron microscopy. As shown in Figure S8a, the Zn deposit surface at 25 °C exhibits a relatively rough and loose feature, with numerous irregular plate-like or flower-like crystal stacks and visible gaps and voids between crystals. This open structure indicates that the reduction kinetics of Zn ions are relatively fast at ambient temperature, leading to preferential growth along specific crystallographic planes, forming larger grains and thereby reducing the compactness of the deposit layer. In contrast, when the temperature decreases to −60 °C, the microstructure of the Zn deposit undergoes a significant transformation, exhibiting a remarkably smooth and dense morphology (Figure S8b). The coarse plate-like structures disappear and are replaced by fine, uniform, and closely packed nanoscale grains. This dense "cobblestone" morphology indicates that the ultra-low-temperature environment effectively suppresses rapid longitudinal growth of Zn dendrites, promoting increased nucleation sites while reducing grain size. The reduced deposition rate and increased nucleation overpotential at −60 °C favor a higher nucleation density and suppress large-scale longitudinal growth, producing finer and denser Zn deposits, thereby filling grain boundary voids and forming a more robust and void-free deposit layer, which is crucial for enhancing cycling stability under extreme conditions.

Just Accepted

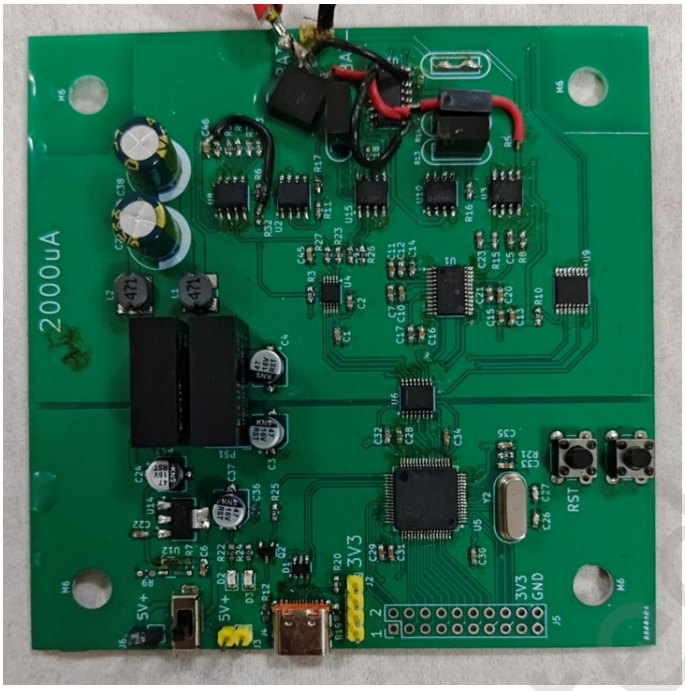


Figure S9. Energy management module in the integrated photovoltaic energy-storage power-supply system.

Just Accepted